Gondwana Research 151 (2026) 390–408

Contents lists available at ScienceDirect

Gondwana Research

journal homepage: www.elsevier.com/locate/gr

Research Paper

Tomographic constraints on the collision boundary between the Yangtze Block and the Sino–Korean Craton and Yellow Sea Basin extension

Yanbing Liu [a], Tae-Kyung Hong [a,*], Junhyung Lee [a], Seongjun Park [a], Samuel Celis [a], Yuxuan Chen [b], Jeongin Lee [a], Byeongwoo Kim [a]

[a] Yonsei University, Department of Earth System Sciences, 50 Yonsei-ro, Seodaemun-gu, Seoul 03722, South Korea
[b] Beijing Earthquake Agency, Haidian, Beijing 10080, PR China

ARTICLE INFO

Keywords:
P wave tomography
Collision
Extension
Sino Korean craton
Dabie sulu orogen

ABSTRACT

The Triassic collision belt between the Yangtze Block and the Sino–Korean Craton, often considered the Dabie–Sulu Orogenic Belt, may extend to the Korean Peninsula. The precise boundary locations, particularly across the Yellow Sea and Korean Peninsula, are poorly constrained. This study uses an improved double-difference tomography method; 3-D P-wave velocity structures at depths up to 55 km are determined based on data from both Chinese and South Korean stations, achieving a resolution of less than 0.5°. A potential collision front, characterized by high-velocity anomalies, is identified. It aligns with the Sulu Orogenic Belt, passing through the northern Yellow Sea, and extends to the western Korean Peninsula, including the Ongjin Basin, Imjingang Belt, and Hongseong area. Significant low-velocity anomalies extend from the crust of the southern Yellow Sea to the mantle beneath the southwestern Korean Peninsula, including the Okcheon Fold Belt and Jeju Island, suggesting the presence of relatively weak and/or hot material, possibly related to basin extension and mantle upwelling.

1. Introduction

The Triassic collision process between the Yangtze Block (YB) and the Sino–Korean Craton (SKC) is a significant and contentious topic in geological research. More than nine models have been proposed for the collision process in the Yellow Sea area, generally agreeing that the Sulu Orogenic Belt (SOB) and the Tanlu Fault Zone (TFZ) form part of the northern and western boundaries (Yin & Nie, 1993; Xu & Zhu, 1994; Zhang, 1997; Chang & Park, 2001; Xu et al., 2021). Key debates focus on whether the Sulu Orogenic Belt may extend into the Yellow Sea region and possibly further to the Korean Peninsula (KP) (Ree et al., 1996; Wan, 2001). However, the proposed Sulu extension zone lies within the Yellow Sea, at the border of China, South Korea, and North Korea, with average water depths of 55–100 m and an average Holocene sediment thickness of about 15 m (Qing et al., 1989; Yang et al., 2003). In this region, the seismic ray coverage is sparse in previous studies, and direct geological evidence is limited, making verification difficult (Fig. 1b). Significant crustal destruction throughout the entire region has complicated the recognition of the collision front (Zhu et al., 2008; Zhu et al., 2012b). Collecting local seismic event records from all countries surrounding the Yellow Sea region is challenging, resulting in low-resolution imaging. Thus, the collision process between the YB and the SKC requires further investigation and validation.

Several velocity tomography studies partially cover our research area, with findings relevant to this study. Higher crustal velocities are found in the KP, while lower velocities are observed in the southern Yellow Sea (Xu et al., 2009; Hao et al., 2013; Wang et al., 2017a; Huang et al., 2023). In the Bohai Sea, low velocities are present in the shallow crust, alternating with high velocities in the mantle, followed by low velocities at greater depths (Feng et al., 2022; Li et al., 2022). In the eastern SOB, low-velocity anomalies are noted, while high-velocity anomalies are observed in the Subei Basin and western SOB. The middle crust of the SOB features thin, low-velocity anomalies, referred to as a “crocodile mouth” structure (Xu, 2001; Wang et al., 2013). Distinct velocity structures exist in the southeastern and northwestern parts of the KP, divided by the South Korea Tectonic Line (Li et al., 2007; Hong & Kang, 2009; Kim et al., 2017a). Beneath Jeju Island, a low-velocity anomaly is found at shallow crust and mantle depths (Song et al., 2018). Additionally, a prominent mid-crustal detachment zone is identified along the TFZ (Lü & Lei, 2022). Other studies, including

* Corresponding author.
E-mail address: tkhong@yonsei.ac.kr (T.-K. Hong).

https://doi.org/10.1016/j.gr.2025.11.006
Received 28 November 2024; Received in revised form 18 October 2025; Accepted 10 November 2025
Available online 5 December 2025

attenuation, gravity, and magnetotelluric (MT) research, indicate low attenuation in most regions of the KP, except the southeast, with high attenuation in the Bohai Sea and western southern Yellow Sea (Hong, 2010; Zhao et al., 2013). High conductivity is observed in the YB and North China Craton (NCC), contrasting with low conductivity in the SOB (Xiao et al., 2009; Ye et al., 2021). Furthermore, low density in the Bohai Sea, Yellow Sea Basin, and eastern SOB is contrasted with high density along the TFZ (Xu et al., 2016b; Hao et al., 2023).

However, a high-resolution velocity structure around the southern Yellow Sea from local body wave arrival times is not yet available. Some ocean bottom seismometer (OBS) surveys with restricted availability have been conducted in parts of the Yellow Sea, providing insights into the crustal structure of certain local depth profiles (Xu et al., 2009; Zou et al., 2016; Kim et al., 2019; Zhang et al., 2021; Zhang et al., 2022; Zhao et al., 2024; Liu et al., 2025). Our local body-wave tomography, by contrast, resolves large-scale structures across the entire region. Local P-wave arrival times with lower picking errors, from densely distributed stations in both China and South Korea, are used. The seismic rays extensively cover both the Yellow Sea region and the eastern SKC, enabling clear and reliable velocity structures to be obtained. The inverted velocity model may constrain the structural boundaries in the region.

2. Geology

The Sino–Korean Craton (SKC) is a Precambrian craton that experienced the amalgamation of the West Block (WB) and East Block (EB) along the Central Orogenic Belt (COB) (Trumbull et al., 1992; Kusky & Li, 2003; Rogers & Santosh, 2006; Zheng et al., 2009; Zhao et al., 2012; Kusky et al., 2016). Following its formation, the craton collided with a northern arc terrane, leading to the development of the Central Asian Orogenic Belt (CAOB), also known as the Inner Mongolia Orogenic Belt (Fig. 1a) (Lu et al., 2006; Zhao et al., 2011; Liu et al., 2017). From the Mesoproterozoic to the mid-Ordovician, the craton experienced a series of extensional and accretionary events but remained relatively stable (Griffin et al., 1998; Kusky, 2011).

However, from the Paleozoic to the Cenozoic, the mantle root of the EB was delaminated, causing significant crustal deformation and lithospheric thinning (Wu, 2011; Zhu et al., 2012b; Wang et al., 2023). Typically, a stable craton has a lithospheric thickness of greater than 200 km, but in the EB, the lithosphere is significantly thinner, about 60–100 km, with a Moho depth of around 30 km (Chen et al., 2006; Ge et al., 2011; Zhang et al., 2019; Zheng et al., 2020). It is suggested that mantle upwelling caused a prolonged and intense decratonization process in the EB (Niu, 2005; Wu et al., 2008; Zhu et al., 2011; Liu et al.,

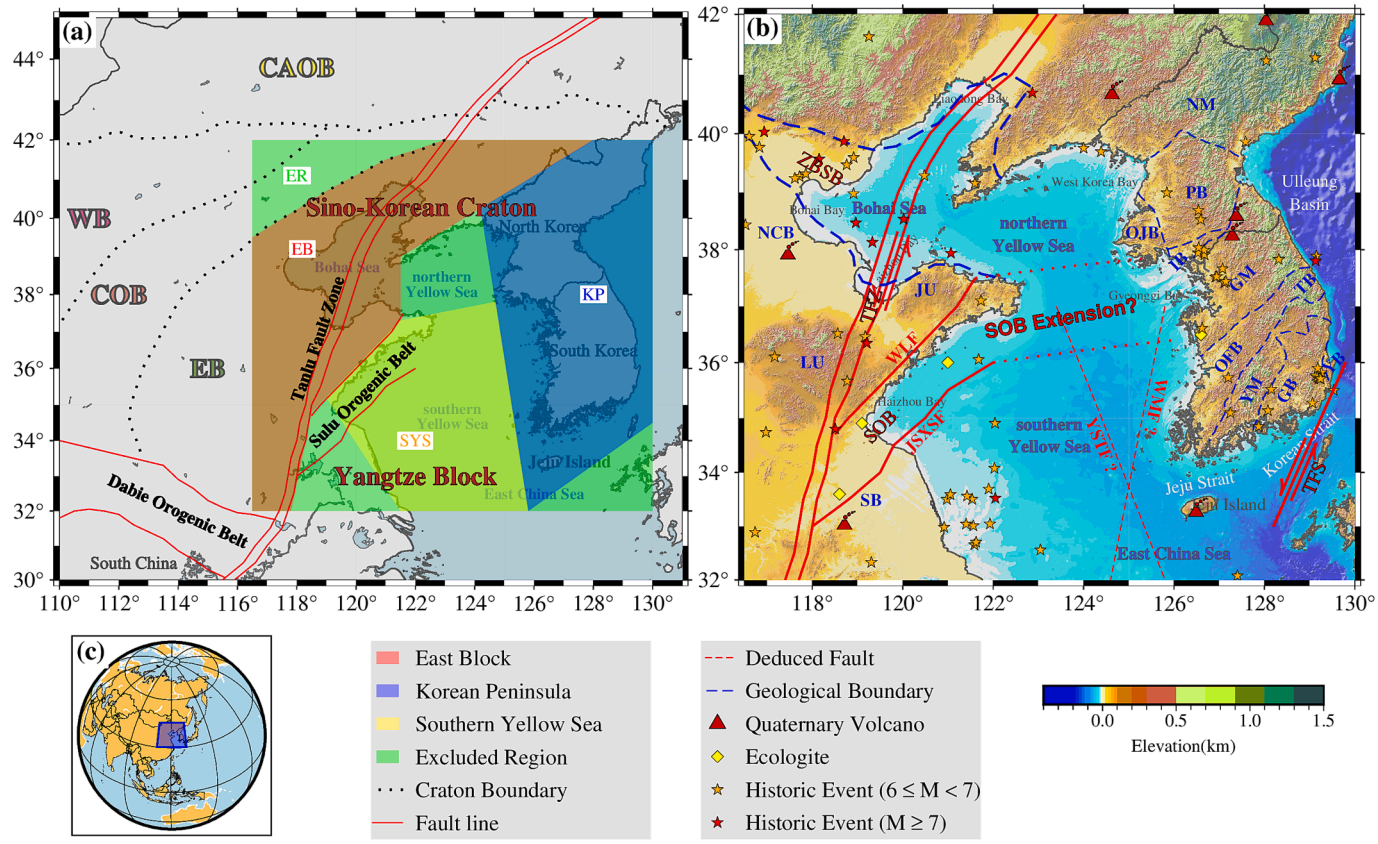

Fig. 1. (a) Main tectonic setting of the Sino–Korean Craton and its surrounding areas. The major blocks of the Sino–Korean Craton include the West Block (WB), East Block (EB), Central Orogenic Belt (COB), and the Central Asian Orogenic Belt (CAOB). The colored regions highlight the subregions used for 1-D velocity inversion, approximately corresponding to the East Block, Korean Peninsula, southern Yellow Sea, and the remaining zones grouped as the 'Excluded Region'. The study area is marked (square box), with craton boundaries (dotted lines) and the subregions for 1-D velocity model inversion are presented. (b) Tectonic map of our study. Geological province boundaries (dashed lines), major faults (solid lines), and deduced faults (dotted lines) are presented. Historical events (M ≥ 6) recorded in China since 800 BCE (stars) (Gu, 1983), historical events (M ≥ 6) recorded in Korea (stars) (KMA, 2012), quaternary volcanoes (volcano symbols) (Lee et al., 2011), and the distribution of eclogites (diamonds) are marked (Yin et al., 2016). The major geological provinces of Korea include the Nangrim Massif (NM), Gyeonggi Massif (GM), Yeongnam Massif (YM), Pyeongnam Basin (PB), Ongjin Basin(OJB), Taebaeksan Basin (TB), Gyeongsang Basin (GB), Yeonil Basin (YB), Okcheon Fold Belt (OFB), and Imjingang Belt (IB) (Lee, 1987; Chough et al., 2000; Park et al., 2023). Some major geological provinces in China include the North China Basin (NCB), Jiaodong Uplift (JU), Luxi Uplift (LU), and Subei Basin (SB). Some major tectonic structures include the Zhangjiakou–Bohai Seismic Belt (ZBSB), Tanlu Fault Zone (TFZ), Sulu Orogenic Belt (SOB), and Tsushima Fault System (TFS). Some existing or deduced faults include the Wulian Fault (WLF), Jiashan–Xiangshui Fault (JSXSF), Yellow Sea Transform Fault (YSTF), and West Marginal Fault (WMF) (Zhang et al., 2003; Xu et al., 2016a). (c) Location of the study area on a global map. (For interpretation of the references to colour in this figure legend, the reader is referred to the web version of this article.)

2019). Consequently, Mesozoic and Cenozoic volcanic activity in this region was particularly intense, leading to the widespread distribution of various types of igneous rock (Chen et al., 2007; Zhu et al., 2008; Pang et al., 2017b; Yang et al., 2019). Geophysical research indicates the presence of low-velocity, high-attenuation, high-conductivity and high heat flow anomalies in the EB's crust (Fang et al., 2013; Zhao et al., 2013; Chen et al., 2014; Zhao et al., 2018; Jiang et al., 2019; Ma et al., 2022). Most studies suggest that this deformation may have been driven by the subduction of the Paleo–Pacific Ocean plate, with the collision between the SKC and the South China Craton (SCC) potentially exacerbating this process (Li, 1994; Shen et al., 2023; Wong, 1929).

It is widely accepted that a paleo-ocean once existed between the SKC and the SCC, commonly referred to as the Mianlue Ocean, with substantial geological evidence supporting its existence (Meng et al., 1999; Xu et al., 2008; Yang et al., 2015; Li et al., 2023). The observation of a large-scale high-velocity body in the north of the Dabie Orogen is commonly interpreted as a remnant of the subducted Mianlue Ocean (Xu et al., 2000a; Xu, 2001; Xu & Zhao, 2009; Ye et al., 2021; Luo et al., 2022). By the Triassic period, the closure of the Mianlue Ocean led to the collision between the northern part of the SCC, namely the Yangtze Block (YB), and the SKC (Xu et al., 2000b; Wang & Lin, 2002; Hacker et al., 2004). This collision resulted in the formation of the Qinling-Dabie-Sulu Orogenic Belt. Geological evidence suggests that the ultra-high-pressure metamorphic rocks in this belt originated from a subduction and exhumation process (Li et al., 2000; Chen & Zheng, 2013; Yin et al., 2016). This feature is strong evidence for subduction preceding the collision. Subsequently, the Tanlu Fault Zone was developed, resulting in the separation of the Dabie and Sulu orogenic belts (Yin & Nie, 1993; Qiao & Zhang, 2002; Zhu et al., 2010). The effects of decratonization were much more severe during this period, primarily affecting the EB (Zhu et al., 2012a).

As a constituent of the SKC, the tectonic evolution of the Korean Peninsula (KP) exhibits broad similarities to that of the North China Craton (NCC) (Chough et al., 2000; Zhai et al., 2019). From the Neoproterozoic through the Middle Paleozoic, evidence of arc-related magmatism preserved in KP's Archean–Paleoproterozoic gneiss basement aligns with records on the NCC (Oh et al., 2006; Zhai, 2016; Kim et al., 2017b). Late Ordovician rift volcanism in the Taebaeksan Basin corresponds to similar rifting-related volcanism in the NCC (Choi, 2014; Lee et al., 2021). Cambro–Silurian arc complexes and Middle Paleozoic amphibolite–granulite P–T paths in KP correspond to metamorphic episodes recorded in the Northern Qinling–Dabie Orogen (Kim et al., 2017b; Song et al., 2020; Lee et al., 2024). In the Triassic, high-pressure metamorphism in the Imjingang–Hongseong area is comparable to that in the Dabie–Sulu Orogenic Belt (Ree et al., 1996; Oh et al., 2005; Sajeev et al., 2010). Amphibolite- to granulite-facies overprints, granitoids, and mixed-Hf zircon plutons testify to synchronous convergence and magmatic pulses (Zhai et al., 2007; Chang & Zhao, 2012; Cheong et al., 2018). During the Mesozoic, right-lateral ductile shearing of the Honam Shear Zone parallels contemporaneous ductile deformation in the NCC (Uno et al., 2004; Cheong et al., 2006; Kim et al., 2009). Cretaceous rifting of the Gyeongsang Rift and pull-apart basins in KP corresponds to back-arc extension in NCC arc systems (Chough et al., 2000; Kim et al., 2012). Studies indicate that widespread lithospheric thinning and delamination, recorded by high-temperature spinel peridotite xenoliths, also occurred in KP, accompanying rejuvenation, renewed magmatism, and basin development (Yang et al., 2010; Zhai, 2016).

3. Data

We collect seismic records of 680 permanent seismic stations in China, provided by the China Earthquake Administration (CEA) from 2008 to 2023, and records from 480 permanent seismic stations in South Korea, provided by the Korea Meteorological Administration (KMA) from 2017 to 2023 (Fig. 2a). The CEA network covers mainland China and surrounding areas, including the Yellow Sea region and several

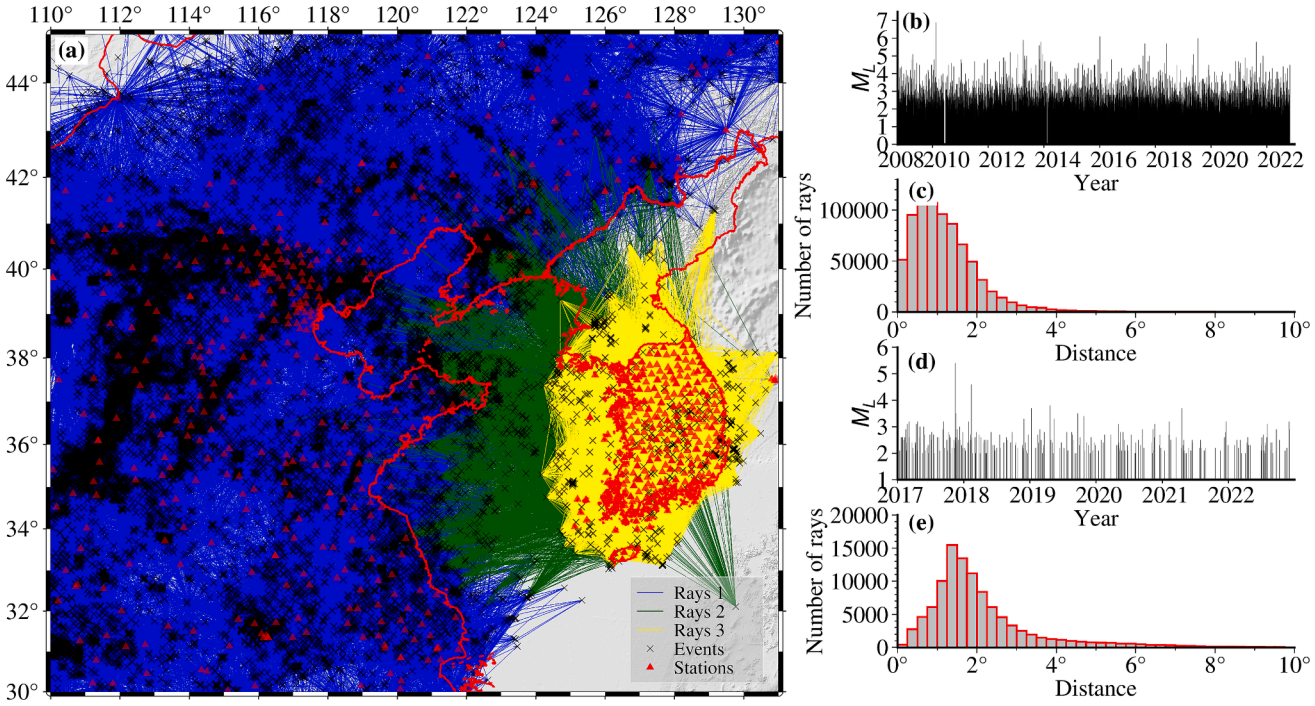

Fig. 2. (a) Ray paths of seismic records used in this study. Earthquakes (crosses) and stations (triangles) are marked. Rays 1 (blue lines) indicate ray paths of events recorded by CEA; Rays 2 (yellow lines) indicate local events recorded by KMA; Rays 3 (green lines) indicate events around Korea recorded by KMA. (b) Temporal magnitude variation of events recorded by CEA. (c) Epicentral distance of events recorded by CEA. (d) Temporal magnitude variation of events recorded by KMA. (e) Epicentral distance of events recorded by KMA. (For interpretation of the references to colour in this figure legend, the reader is referred to the web version of this article.)

large earthquakes on the Korean Peninsula, whereas the KMA network primarily covers the Korean Peninsula and adjacent regions. A total of 900 local events with local magnitudes greater than 2 recorded by the dense Korean stations are selected, and 63,253 events with local magnitudes greater than 1 in China are used to enhance ray path density. For the Yellow Sea region, located between the two networks, 1,580 events with local magnitudes greater than 2 are used in this study as they generate relatively clear seismic phases. The epicentral distances are less than 2000 km (Fig. 2b).

We perform a two-step relocation, with both steps relying on P-wave first arrivals from local events. In tomographic analyses, we include Pg, Pn, and later Pg arrivals. For CEA data, phase reports are used, whereas for the KMA waveform data, arrival times are manually selected with the assistance of a machine learning algorithm, PhaseNet (Zhu & Beroza, 2019). We used the original PhaseNet model trained on the Northern California earthquake dataset to pick arrival times from KMA data, then applied transfer learning using our manually picked arrival times to further optimize the model. PhaseNet typically selects the component with the highest probability of three components of an event, which may not always correspond to the first arrival. To address this, some minor improvements are made to prioritize selecting the first arrival among the three components. After testing, the final picking error (difference between PhaseNet picks and manual picks) is within 0.5 s. However, manual selection is indispensable to obtain arrival times with lower error. While the machine learning-based PhaseNet algorithm is trained, optimized, and tested in this study, all final arrival times are manually picked.

After meticulous selection and removal of outliers, the final dataset includes 678,579 Pg arrival times and 82,234 Pn arrival times from CEA records, and 55,813 Pg arrival times and 34,047 Pn arrival times from local event records of KMA. Additionally, for events around the eastern SKC recorded by KMA, there are 3,893 Pg arrival times and 8,994 Pn arrival times. The traveltime curves of these six datasets are presented (Fig. 3). It is noteworthy that when traveltime curves are used to screen the data, the selection of cutting thresholds is crucial. The L-curve method is employed to determine the best cutting thresholds. For each of the six datasets, L-curve calculations with the decrease in the number of arrival times as the independent variable and the cutting range as the dependent variable were performed to determine their optimal cutting thresholds (Fig. S1 in the Supplementary Materials). The results of the L-curve analysis indicate that the manually picked phase arrival times from the South Korean data set have higher accuracy, and most arrival times are retained.

4. Methods

One-dimensional (1-D) velocity models are commonly used to construct initial models for relocation and tomography. Well-established 1-D global average models, such as CRUST1.0 and IASP91 (Kennett & Engdahl, 1991; Laske et al., 2013), and the regional three-dimensional (3-D) lithospheric model USTClitho2.0 for continental China and adjacent areas (Han et al., 2021) can be referenced, although their accuracy may be limited at local scales. Alternatively, seismic profiles or receiver function results from past research may not fully match the study area. A more optimal approach is to extract the 1-D model from the given data. VELEST (Kissling, 1988; Kissling et al., 1994) allows for joint inversion of earthquake locations and velocity models using layered ray tracing to obtain the best-fit 1-D model (Crosson, 1976), which can be used for initial models in event relocation and traveltime tomography (Thurber, 1981; Kissling & Lahr, 1991). The underlying principles are presented in Section S2 in Supplementary Materials.

Achieving a global minimum requires iterative inversions of large datasets. This study enhances the program capacity to process large datasets. We introduce a multiple inversion and residual comparison workflow to ensure that the final inverted velocity model converges to a stable global minimum (see, Section S3 and Fig. S2 in Supplementary Materials).

We apply the double-difference method to conduct event relocation and traveltime tomography. The residual between the observed traveltime and the theoretical traveltime can be expressed as (Waldhauser & Ellsworth, 2000),

$$r_k^i = \sum_{l=1}^{3} \frac{\partial t_k^i}{\partial X_l^i} \Delta X_l^i + \Delta t_o + \int_i^k \delta u ds, \tag{1}$$

where, r_k^i is the residual from events i to station k, u is the slowness, X represents the location of event (x, y, z), for the same station k, and the difference in residuals between two events i and j, known as the double-difference Dr_k^{ij} is

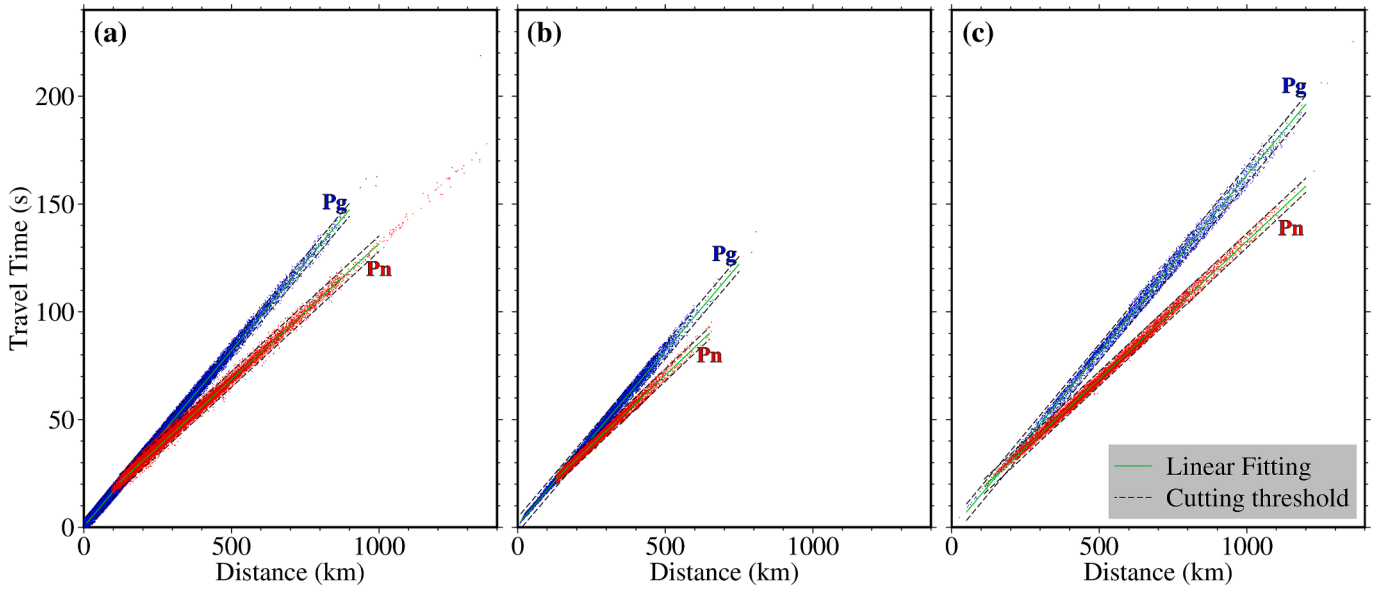

Fig. 3. Traveltime curves of all six datasets. The cutting thresholds (dashed lines) and the linear fitting lines (solid lines) are presented, the Pg and Pn arrival times (points) are marked. (a) Arrival times recorded by CEA. (b) Arrival times of local events recorded by KMA. (c) Arrival times near Korea recorded by KMA.

$$Dr_k^{ij} = r_k^i - r_k^j = \sum_{l=1}^{3} \frac{\partial t_k^i}{\partial X_l^i} \Delta X_l^i + \Delta t_o^i + \int_i^k \delta u ds - \sum_{l=1}^{3} \frac{\partial t_k^j}{\partial X_l^j} \Delta X_l^j$$

$$+\Delta t_o^j - \int_j^k \delta u ds \quad (2)$$

When the distance between these two events is sufficiently small, their raypaths to common stations are approximately the same. Equation (2) can be simplified to be

$$Dr_k^{ij} = r_k^i - r_k^j = \sum_{l=1}^{3} \frac{\partial t_k^i}{\partial X_l^i} \Delta X_l^i + \Delta t_o^i - \sum_{l=1}^{3} \frac{\partial t_k^j}{\partial X_l^j} \Delta X_l^j + \Delta t_o^j \quad (3)$$

The double-difference method (TomoDD) determines both relative and absolute positions and velocity structures (Zhang & Thurber, 2006). In this study, we separate event relocation and traveltime tomography into two stages. In the relocation stage, we first use VELEST with high-precision P-wave first-arrival times from local events to invert 1-D velocity models and perform an initial relocation of hypocenters. We then interpolate the VELEST-generated 1-D models to build the 3-D initial model for the TomoDD relocation. Next, we apply TomoDD's standard algorithm using the VELEST-derived 3-D initial model and those same high-quality first arrivals to further refine hypocenter positions. The resulting 3-D velocity model from the TomoDD relocation step then serves as the initial 3-D model for tomography. In the tomography stage, we fix the well-relocated hypocenters and incorporate all reliable Pg and Pn traveltime data, including later Pg arrivals. The standard TomoDD implementation processes only first arrivals and thus cannot exploit later Pg phases (Sun, 2019). Our ray tracing in the tomography step follows TomoDD's pseudo-bending approach with the TomoDD-SR enhancement, which constrains later-Pg raypaths to remain within the crust, thereby preventing their mis-tracking as Pn waves, by prescribing a constant mantle velocity below the Moho during the later-Pg ray-tracing (Sun et al., 2021a; Sun et al., 2021b). Further information on the TomoDD-SR method is provided (see, Section S6 in the Supplementary Materials).

The flow chart for relocation and tomography is shown (Fig. S3 in Supplementary Materials). Statistical characteristics of traveltime residual histograms at different inversion stages are provided (Fig. S21).

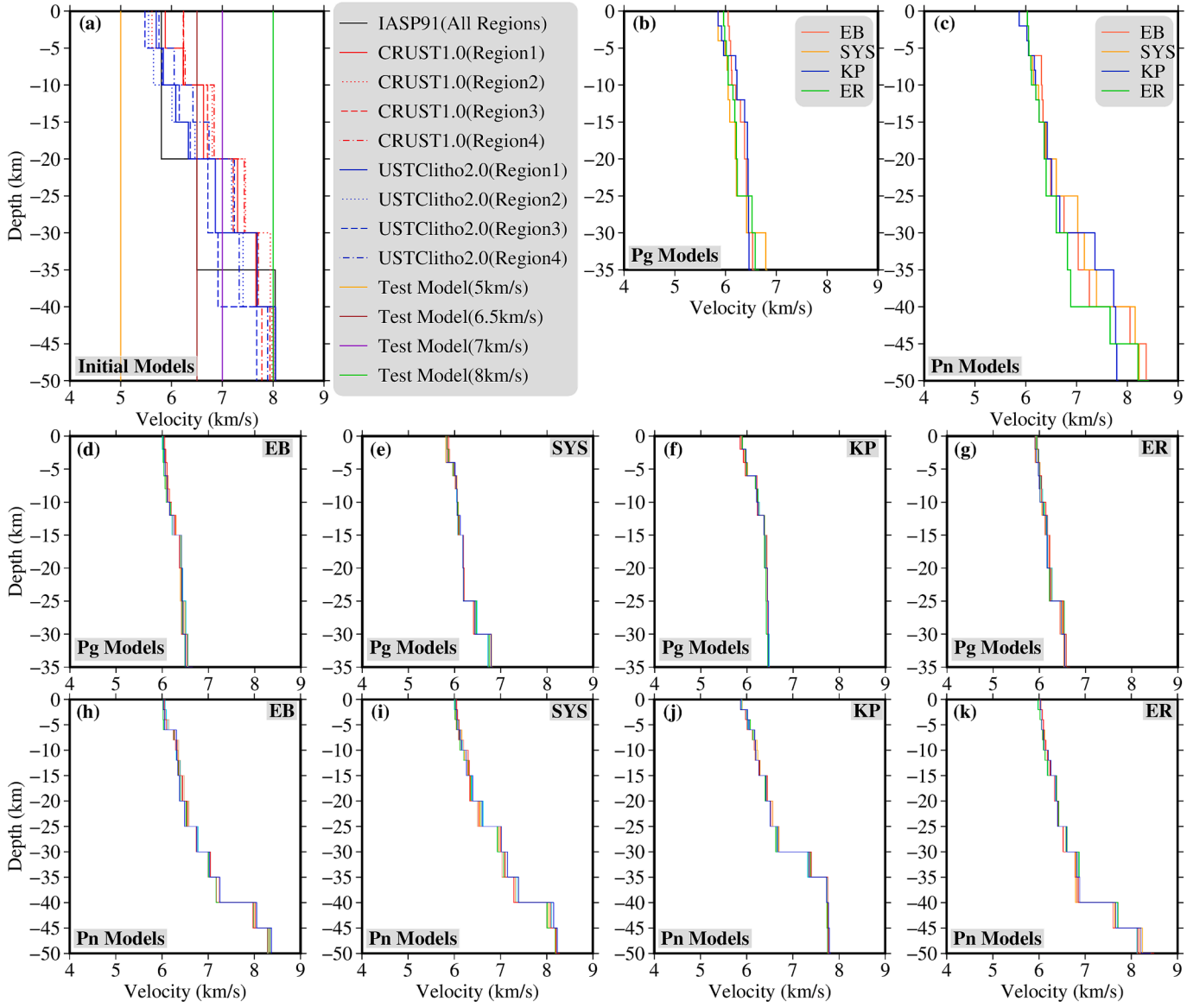

Fig. 4. 1-D velocity models. (a) Seven initial models used for inversion in each region. (b) The final 1-D Pg models of different regions. (c) The final 1-D Pn models of different regions. (d)–(g) The inverted 1-D Pg models with different initial models in different regions. (h)–(k) The inverted 1-D Pn models with different initial models in different regions.

The VELEST-inverted 1-D models used to create the 3-D models for the TomoDD relocation step are presented (Table S1 in Supplementary Materials). A schematic illustration of the theoretical ray paths in the tomography step is shown (Fig. S4 in Supplementary Materials). The appropriate damping value and weighting parameters for the tomography inversion are determined using the L-curve method (see, Section S5 and Fig. S5 in Supplementary Materials).

We assess the cell-hit counts using the derivative weighted sum (DWS), which is the sum of the partial derivatives of traveltimes with respect to slowness (see, Section S4 in Supplementary Materials) (Thurber & Eberhart-Phillips, 1999). The DWS distribution maps for each depth assess ray density through grid nodes (Fig. S6 in Supplementary Materials). In most regions, DWS values exceed 100, while areas with DWS values below 10 are excluded from the tomography analysis. Additionally, we select seismic events that are recorded in at least eight stations. Each station records a minimum of five events with traveltime residuals less than 3 s.

5. Average 1-D velocity models, event relocation and seismicity

5.1. Average 1-D velocity models

The eastern Sino–Korean Craton (SKC) is divided into four subregions: East Block (EB), southern Yellow Sea (SYS), Korean Peninsula (KP), and an excluded region (ER) (Fig. 1a). These areas display distinct geological backgrounds, significant velocity variations, and different Moho depths, necessitating separate 1-D velocity model inversions and event relocations.

Seven initial models, including CRUST1.0, IASP91, and USTClitho2.0, yield consistent 1-D models for Pg and Pn waves across the subregions (Fig. 4). To assess the robustness of the 1-D velocity model, we perform a bootstrap test based on 100 datasets, following the nonparametric approach (Efron & Tibshirani, 1991). Each dataset is compiled from the original catalog, with events resampled allowing for multiple selections. The number of events is the same as in the original catalog. All associated phase arrivals for each selected event are retained, and the inversion parameters are fixed across iterations. The 100 resulting velocity models are used to estimate the median and 95 % confidence interval at each depth. Bootstrap tests confirm inversion stability, with all tests showing consistent results within a 95 % confidence interval (Lamarre et al., 1992; Hong & Menke, 2008). The inversion presents velocity variations of ± 0.03 km/s for depths less than 25 km and ± 0.05 km/s for greater depths (Fig. S7 in Supplementary Materials).

Fitting travel-time curves across the study area suggests average Pg and Pn velocities of 6.13 and 7.04 km/s, respectively. Below, we present absolute velocities and their deviations from the VELEST-inverted 1-D model. Pg deviations are referenced to the regional average Pg velocity (6.13 km/s), and Pn deviations to the regional average Pn velocity (7.04 km/s).

For inverted Pg models, the SYS region exhibits velocities of 5.85–6.21 km/s at depths of 0–25 km, deviating −4.6 % to + 1.3 %, and 6.79 km/s at 30–35 km, deviating + 10.8 %. The KP region shows 5.85–5.92 km/s at 0–5 km (−4.6 % to −3.4 %), 6.20–6.44 km/s at 5–25 km (+1.1 % to + 5.1 %), and 6.46 km/s at 30–35 km (+5.4 %). The Pn model for the KP region presents velocities of 7.36–7.73 km/s at 30–40 km (+4.6 % to + 9.8 %) and 7.77–7.79 km/s at 40–50 km (+10.4 % to + 10.6 %). The SYS region shows 7.15–7.39 km/s at 30–40 km (+1.6 % to + 5.0 %) and 8.15–8.23 km/s at 40–50 km (+15.8 % to + 16.9 %).

Comparatively, the SYS region exhibits the lowest Pg velocities at 0–25 km and the highest at 30–35 km. The KP region shows relatively low Pg velocities at 0–5 km, the highest at 5–25 km, and lower values than SYS at 30–35 km. KP exhibits the highest Pn velocities at 30–40 km, with slightly lower values at 40–50 km compared to its shallower layer. SYS shows intermediate velocities at 30–40 km, lower than KP but higher than other regions, and the highest velocities among all regions at 40–50 km.

5.2. Event relocation and seismicity

We refine event locations using the VELEST method with high-quality near-field P-wave first arrivals. Subsequently, the TomoDD method is applied for secondary relocation, ensuring that all events, including those removed during event pairing, are relocated. This process produces a complete catalog, with only a few events not relocated. The distribution of relocated and historical events is shown in Fig. 5.

To better illustrate the relocation results, we add supplementary information on six representative examples in the Supplementary Materials (Figs. S8–S14). Fig. S8 shows the RMS reduction during the iteration process, while Figs. S9–S14 display the relocated seismic clusters. The hypocentral locations are well constrained through relocation, and the relocated events show good spatial correlation with geological structures, with most earthquakes concentrated along fault zones.

The seismicity density map shows the distribution of relocated events (Fig. 6b). Two main active zones are identified. One is the aftershock region of the 1975 Ms7.3 Haicheng earthquake. It trends northeast along major faults. The other is the Zhangjiakou–Bohai Seismic Belt (ZBSB), which includes significant historical events such as the 1976 Ms7.8 Tangshan earthquake. Two moderately active zones are also apparent. One is in the southern Yellow Sea, where more than 15 earthquakes of Ms ≥ 6 have been recorded, along with one Ms7.0 event. The other is on the southeastern Korean Peninsula, which has experienced more than six events of Ms ≥ 6, including one Ms7.0 event (the 1681 Jumunjin earthquake). The current seismicity-active region is mainly concentrated around these Ms ≥ 6 events (Huang et al., 1996; Lee & Kim, 2002; Liu et al., 2013; Shen et al., 2014; Park et al., 2021).

The southern segment of the Tanlu Fault and the west coast of the Korean Peninsula, while historically prone to large earthquakes, now exhibit low seismicity. The Tanlu Fault Zone is a discordogenic fault zone formed during the collision between the Yangtze Block and the Sino-Korean Craton. Initially a dextral strike-slip fault, it later incorporated reverse and sinistral strike-slip components (Peng et al., 2022). The Tanlu Fault experienced multiple Ms7 events before the 1800s (Events 1, 4, and 3 in Fig. 6b), but is currently quiet, with major events now only occur at its intersection with the ZBSB (Zhang et al., 1985; Zhu et al., 2018). A similar situation is observed along the west coast of the Korean Peninsula, which some suggest may serve as a structural boundary during collision (Hao et al., 2002; Chang, 2015; Hu et al., 2022a). However, current seismicity levels are moderate to low, questioning this classification. Despite a history of numerous earthquakes of Ms ≥ 6, the western margin has been notably quiet since the 1800s, similar to the Tanlu Fault Zone.

6. Resolution test

The checkerboard resolution tests are conducted to examine the resolution of the inverted P wave models (Lévêque et al., 1993; Rawlinson & Spakman, 2016). The input model covers the region from 117°E to 130°E and 32°N to 42°N, with a vertical extent down to 60 km, consistent with the model space used in our tomography inversion. Since the earthquake locations were already accurately determined during the TomoDD relocation step using high-quality near-field P-wave first arrivals, we fixed the event locations during the tomography inversion. Accordingly, the checkerboard resolution tests were also conducted with fixed event locations.

The synthetic model generates theoretical arrival times by imposing checkerboard velocity anomalies with a uniform size of 0.5° × 0.5° × 4 km (Fig. 7), aligning with the inversion grid. The theoretical arrival times share the same event-station distribution as the real data, with relative velocity perturbations of ±8 %. The same inversion strategy and parameters apply, incorporating Gaussian white noise of approximately

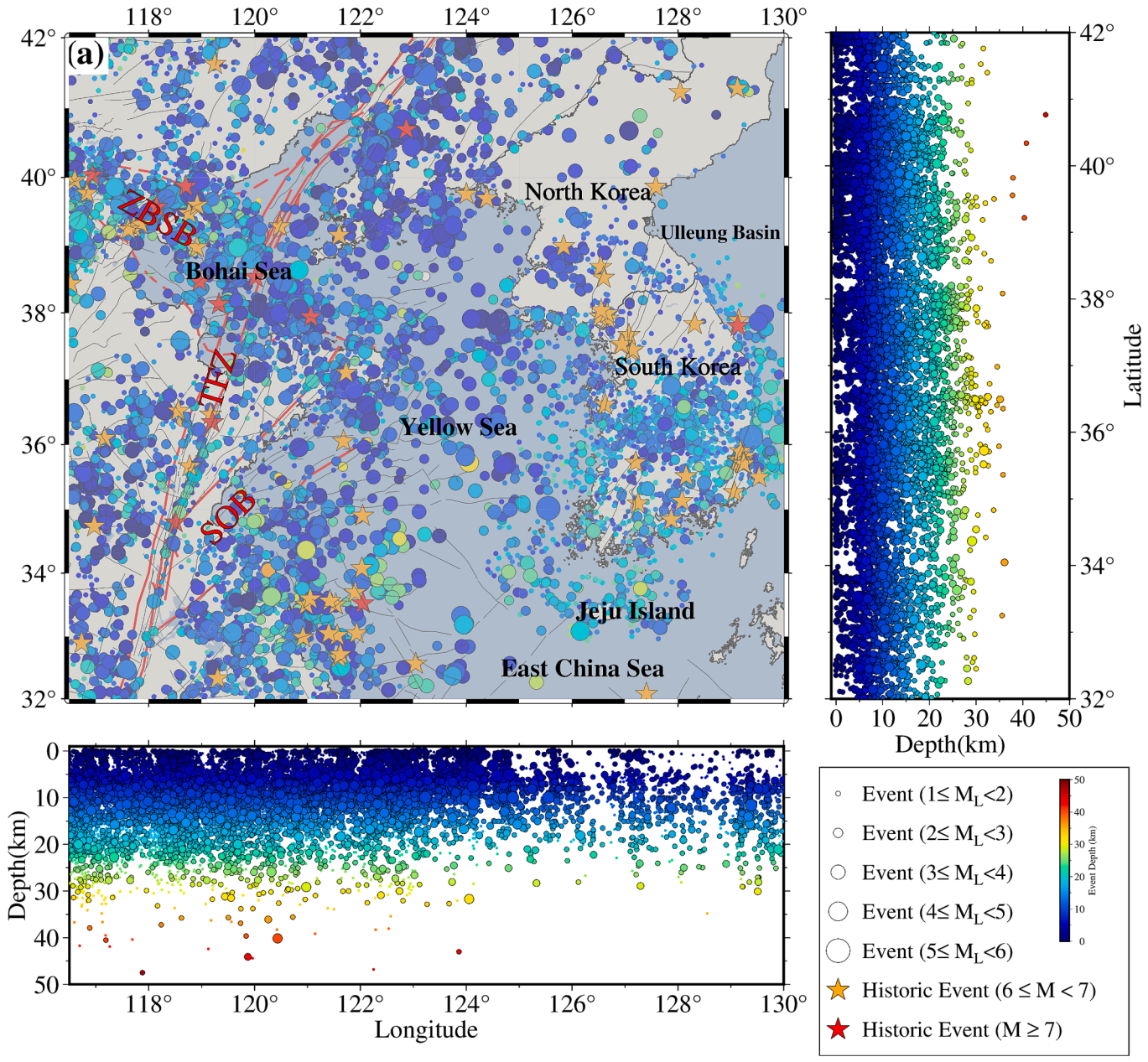

Fig. 5. Distribution of relocated events since 2008 and historical events (M ≥ 6) recorded in China since 800 BCE (stars) (Gu, 1983), historical events (M ≥ 6) recorded in Korea (stars) (KMA, 2012).

15 % of the signal to simulate higher traveltime picking errors. Horizontal profiles within the depth range of 5–45 km demonstrate good resolution in most areas, while resolution is low in eastern North Korea and near Japan due to sparse ray coverage. At a depth of 55 km, resolution weakens at the edges of the study area but remains good in the center.

To assess the potential influence of event location uncertainty, an additional test introduces random Gaussian perturbations (±0.2°) to the original hypocenter coordinates, followed by full inversion. The resulting resolution pattern remains largely unchanged, with only slight smearing observed in regions of limited ray coverage (Fig. S15). A coarser checkerboard pattern (1° × 1° × 8 km) is also tested to evaluate large-scale resolving ability. The results indicate that major velocity anomalies discussed in the main text remain well resolved, further supporting the robustness of the inversion (Fig. S16).

The second set of synthetic tests evaluates the resolution and stability of the inversion results for vertical and dipping velocity anomalies (Zhang & Thurber, 2005). The input model simulates four types of laterally extensive low-velocity zones, positioned along latitudes 33.5°, 34.5°, 35.5°, and 36.5° (Fig. S17). Among them, the anomaly at 34.5° is designed to simulate the influence of sedimentary layers in the Yellow Sea. Those models are used to generate synthetic arrival times, with 15 % Gaussian white noise added to simulate traveltime picking errors. Using the same inversion strategy and parameters as in the real-data inversion, the results show that the low-velocity anomalies are well recovered in shape, width, and dip angle across all profiles. In areas with good ray coverage, the inversion has adequate capability to distinguish between the high- and low-velocity structures. This demonstrates effective recovery of the synthetic velocity structures. Vertical smearing remains limited within the depth range of the study.

7. Inverted P velocity models

Horizontal profiles at different depths of the inverted P-wave relative

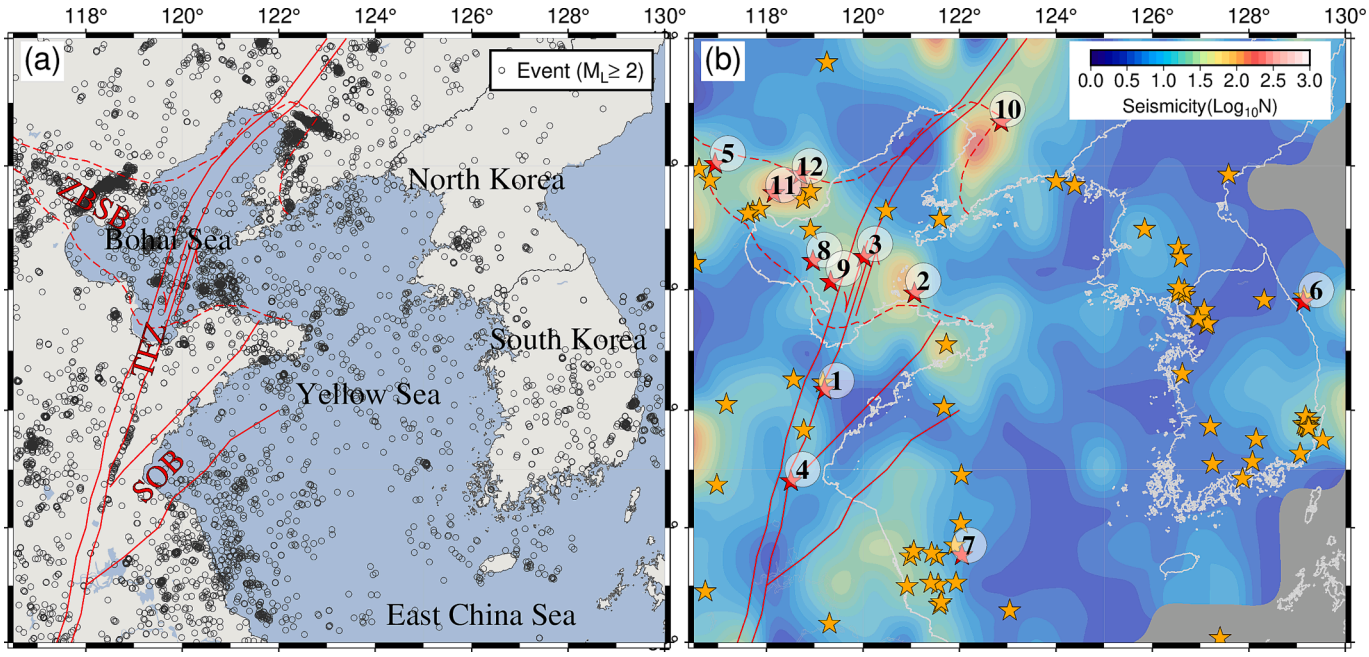

Fig. 6. (a) Earthquake distribution map since 2008 with events larger than local M_L 2.0; (b) Seismicity density map corresponding to (a). Historical events are numbered by their occurrence time, Event 1 to Event 12 represent the following historical earthquakes: Event 1. 70BC Zhucheng Ms7.0, Event 2. 1548 Bohai Ms7.0, Event 3. 1597 Bohai Ms7.0, Event 4. 1668 Tancheng Ms8.5, Event 5. 1679 Sanhe-Pinggu Ms8.0, Event 6. 1681 Jumunjin Ms7.0, Event 7. 1846 southern Yellow Sea Ms7.0, Event 8. 1888 Bohai Ms7.5, Event 9. 1969 Bohai Ms7.4, Event 10. 1975 Haicheng Ms7.3, Event 11. 1976 Tangshan Ms7.8, Event 12. 1976 Tangshan Ms7.1 (Gu, 1983). (For interpretation of the references to colour in this figure legend, the reader is referred to the web version of this article.)

velocity model are presented (Fig. 8). The Moho depth in the study area ranges from depth 27 to 35 km (Chang & Baag, 2007; Choi et al., 2015; Xu et al., 2016b; Zhang et al., 2019). Depth slices from 5 to 25 km mainly represent crustal structures, whereas those between 35 and 45 km are primarily associated with upper mantle features. The 30 km depth profile lies within the estimated Moho depth range, and the observed velocity anomalies at this depth may reflect both crust–mantle transitional structures and lateral variations in Moho topography. The color scale range was set to ±8 %, as over 95 % of the grid nodes exhibit velocity perturbations within this interval (see, Section.S7 and Fig. S18 in Supplementary Materials).

The mantle velocity structure significantly contrasts with the crustal structure. In the crust, the eastern area, including the Korean Peninsula and northern Yellow Sea, exhibits relatively high velocities, while the Bohai Sea and southern Yellow Sea to the west show lower velocities. This trend reverses at mantle depths. Most historical events of Ms7 or higher occurred at the boundaries between high and low-velocity zones at seismogenic depths (5–20 km). Additionally, all Quaternary volcanoes display low-velocity anomalies at both crustal and mantle depths. Below, we describe the velocity anomalies observed in the major tectonic domains, including the Sulu Orogenic Belt, the Tanlu Fault Zone, the Yellow Sea and the Korean Peninsula.

Both the crust and upper mantle beneath the western Sulu Orogenic Belt (SOB) primarily exhibit high P-wave velocities. This structural feature aligns well with the typical characteristics of continental collision zones (Xu et al., 2001; Bai et al., 2007; Zhao et al., 2024). The high-velocity patterns also correspond to the distribution of ultrahigh-pressure metamorphic rocks identified in this region (Zhai et al., 2007; Zhang et al., 2009). The eastern part of the crust, connected to the southern Yellow Sea, exhibits low velocities, which may be related to the extension of the southern Yellow Sea Basin (Pang et al., 2017a). Some localized low-velocity anomalies in the crust have been interpreted as zones of partial melting (Chen & Zheng, 2013; Li et al., 2018).

The northern segment of Tanlu Fault Zone (TFZ) crosses the Bohai Sea Basin and the Zhangjiakou–Bohai Seismic Belt (ZBSB), showing pronounced low velocities in the crust and high velocities in the mantle. This zone is highly seismically active, with more than eight earthquakes of Ms7 or greater. Previous studies have suggested that the low-velocity anomalies are likely linked to basin extension, mantle upwelling, and intense seismic activity (Chen et al., 2006; Huang et al., 2023; Jia et al., 2014; Li, 1994; Li et al., 2022; Ma et al., 2022; Xu et al., 2021). The southern segment crosses the Luxi Uplift and the Subei Basin near the Sulu region, and exhibits high velocities.

The Yellow Sea comprises the northern (NYS) and southern (SYS) subregions, each with distinct geological structures and evolutionary histories (Zheng et al., 2005; Wang et al., 2014). In the NYS, the crust shows high P-wave velocities, while low-velocity anomalies appear in the eastern upper mantle (35–45 km depth; Region C), possibly related to regional magmatic activity (Wang et al., 2017b). The SYS displays a more complex velocity pattern: the western SYS, adjacent to the Chinese mainland, has low crustal velocities and relatively high mantle velocities, while the eastern SYS exhibits the opposite. Shallow low-velocity anomalies in the SYS may reflect thick sedimentary layers (Qing et al., 1989; Yang et al., 2003; Straume et al., 2019), whereas mantle low-velocity anomalies may result from widespread igneous activity and normal and strike-slip faulting related to basin extension (Liang et al., 2003; Zheng et al., 2005; Pang et al., 2017b; Petrishchevsky, 2022). Historical events of magnitude Ms ≥ 6 in the NYS align with the boundaries between high- and low-velocity anomalies at seismogenic depths (10–15 km) (KMA, 2012).

The Korean Peninsula displays contrasting P-wave velocity structures in the crust and mantle. High velocities dominate the crust. Low velocities are prominent in the upper mantle. The Imjingang Belt and Gyeonggi Bay exhibit consistently high velocities in both layers, likely reflecting dense lithologies and strong metamorphism (Zhang, 1997). The Gyeonggi Massif contains distinct low-velocity anomalies at ~10 km depth and in the uppermost mantle (Region A). In this area, two Quaternary volcanoes (Chugaryong and Kilchu-Myongchon), and Late Triassic potassic plutons are present (Whitford-Stark, 1987; Cheong et al., 2018). These anomalies may reflect localized upwelling or the effects of magmatism and back-arc extension (Chough et al., 2018; Song et al., 2020; Hong et al., 2024). The Okcheon Fold Belt (OFB) shows high

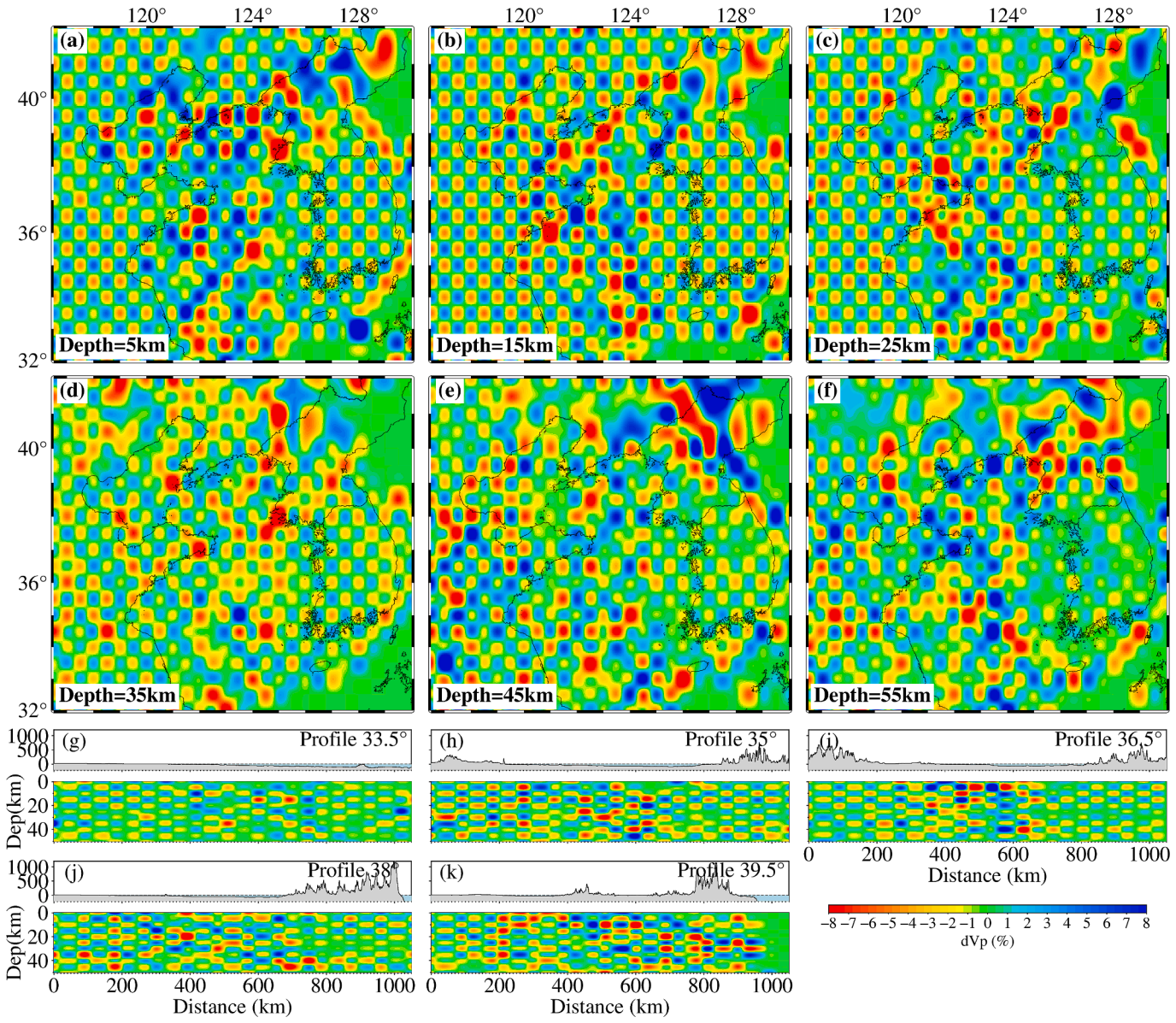

Fig. 7. Resolution test. All images share the same color bar, with P-wave relative velocity perturbations between −8 % and 8 %. (a)–(f) Horizontal resolution test in different depth (5 km, 15 km, 25 km, 35 km, 45 km, 55 km) with cell size of 0.5°. (g)–(k) Vertical resolution test of different latitudinal profiles (33.5°, 35°, 36.5°, 38°, 39.5°) with cell size of 0.5°×4 km.

velocities in the upper to middle crust, with low-velocity anomalies at 25 km and 35–40 km depths, suggesting complex deformation and tectonic stress near the South Korean Tectonic Line (Cho et al., 2008; Choi et al., 2012). The Yeongnam Massif and Gyeongsang Basin share similar patterns of crustal high and mantle low velocities. Jeju Island exhibits shallow (5 km) and deep (35–40 km) low-velocity anomalies (Region B), which may indicate Quaternary volcanism (Brenna et al., 2015; Song et al., 2018). The Nangrim Massif and eastern Pyeongnam Basin display localized low-velocity anomalies in both the crust and the mantle.

8. Vertical cross sections

Vertical profiles of the inverted differential velocity model, along with the absolute velocity model, are presented (Figs. 9 and 10). The range of relative velocity perturbations is consistent with the horizontal profiles and the checkerboard tests. The specific locations of these profiles are presented on the models (Figs. 9a and 10a). The N-S longitudinal profiles (Fig. 9) and the W-E latitudinal profiles intersect the major tectonic units (Fig. 10).

The profiles can be divided into several subregions based on the relative velocity variations along each section. A lateral sliding-window scanning technique is applied along each profile, with a fixed window width of 1° (Liu & Pei, 2017). Within each window, the average relative velocity is calculated over the entire depth range to capture the overall velocity characteristics, as shown in Fig. S12. Zones with average relative velocity values below 0 % are classified as low-velocity regions, and those above 0 % as high-velocity regions. Specifically, values between 0 % and 1 % are defined as weakly low-velocity, and values exceeding the mean of all positive relative velocities across the profile are classified as strongly high-velocity. Accordingly, we apply a unified color scheme in the topographic profile segments of Figs. 9 and 10: light red for weak low-velocity region, red for strong low-velocity, light blue for weak high-velocity, and blue for strong high-velocity.

The region identified as the Triassic collision boundary (BD) generally shows consistent features. In most profiles, it displays high

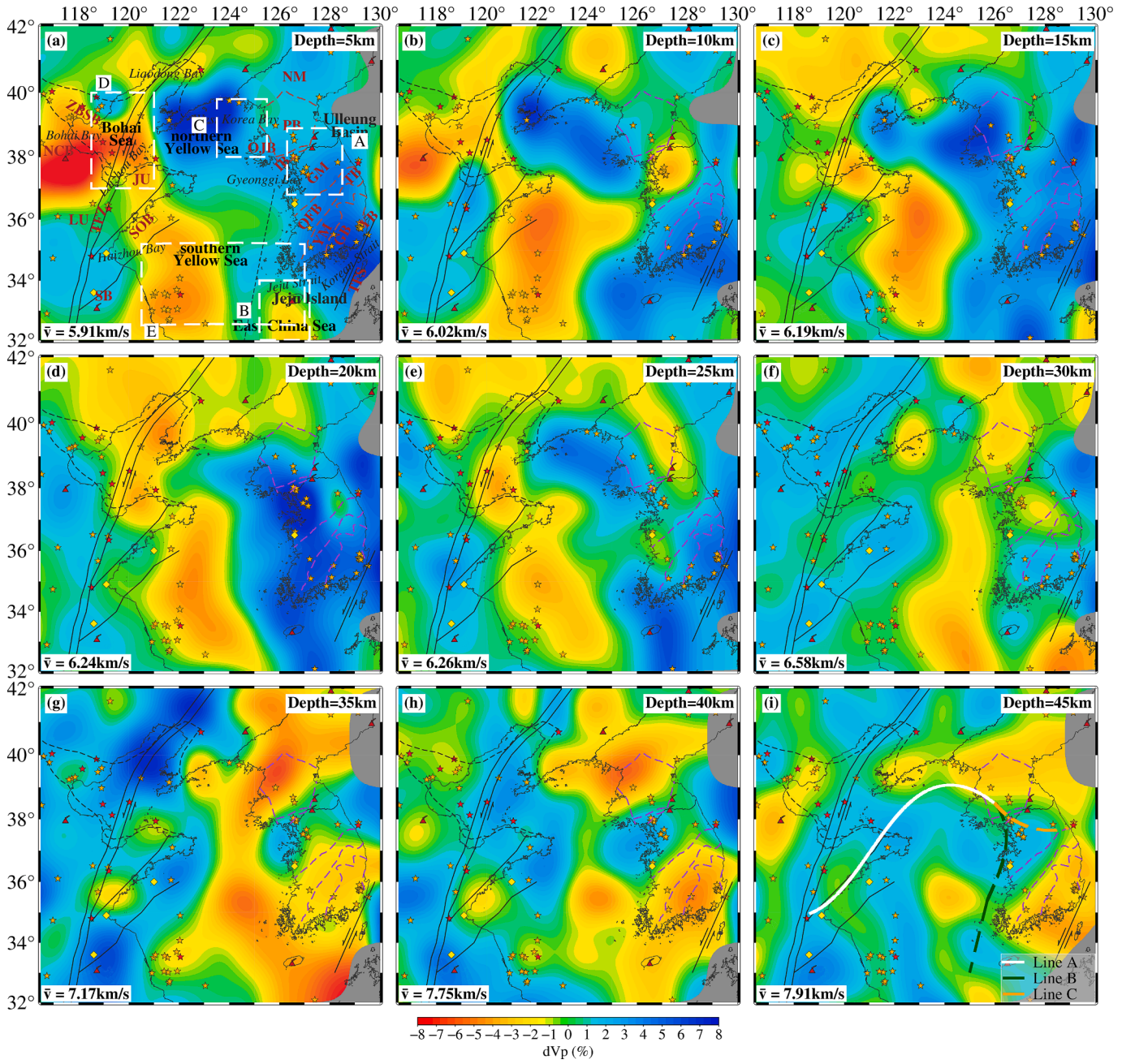

Fig. 8. Differential P-wave velocity maps at different depths. Major geological provinces are marked, with abbreviations consistent with those in Fig. 1. Regions with poor resolution have been removed. Crustal depths: (a)–(e) correspond to 5 km, 10 km, 15 km, 20 km, and 25 km, respectively. Mantle depths: (g)–(i) correspond to 35 km, 40 km, and 45 km, respectively. The average velocity $\bar{v}$ at each depth is indicated in the corresponding panel. Historical events (M ≥ 6) recorded in China since 800 BCE (stars) (Gu, 1983), historical events (M ≥ 6) recorded in Korea (stars) (KMA, 2012), quaternary volcanoes (volcano symbols) (Lee et al., 2011), and eclogite sites (diamonds) are marked (Yin et al., 2016). The relatively well-constrained collision boundary (Line A) and two possible structural boundaries (Lines B and C), as proposed in Fig. 12, are shown in panel (i).

velocities, over 3 % above the average, across the entire crust and uppermost mantle. The only exception is the 36° profile, where the BD shows a very weak low-velocity anomaly, with a maximum deviation of about –0.3 %. In these profiles, the BD contrasts sharply with the surrounding zones that are primarily characterized by low velocities, including the North China Craton (NCC), the Yangtze Block (YZ), and the northern Korean Peninsula, making its northwestern boundary relatively easy to identify. However, in the southern Korean Peninsula, high velocities are also present, making it difficult to determine whether the BD lies within the peninsula or extends into the Yellow Sea. Profile 126° shows a thin low-velocity band at ~10 km depth, resembling the "crocodile mouth" structure noted in previous studies on the Dabie–Sulu Orogenic Belt and possibly caused by partial melting, but its existence requires further validation. (Xu et al., 2000b; Chen & Zheng, 2013; Li et al., 2018).

The velocity profiles reveal significant extensional deformation in the Yellow Sea region. In the longitudinal profile at 123° and the latitudinal profiles from 33° to 36°, the upper and middle crusts exhibit widespread low-velocity anomalies in the southwestern Yellow Sea (Region E). These anomalies extend both laterally and vertically, reaching into the upper mantle beneath the Jeju Volcanic Island, the southern Yeongnam Massif (YM), and the Gyeongsang Basin (GB). A

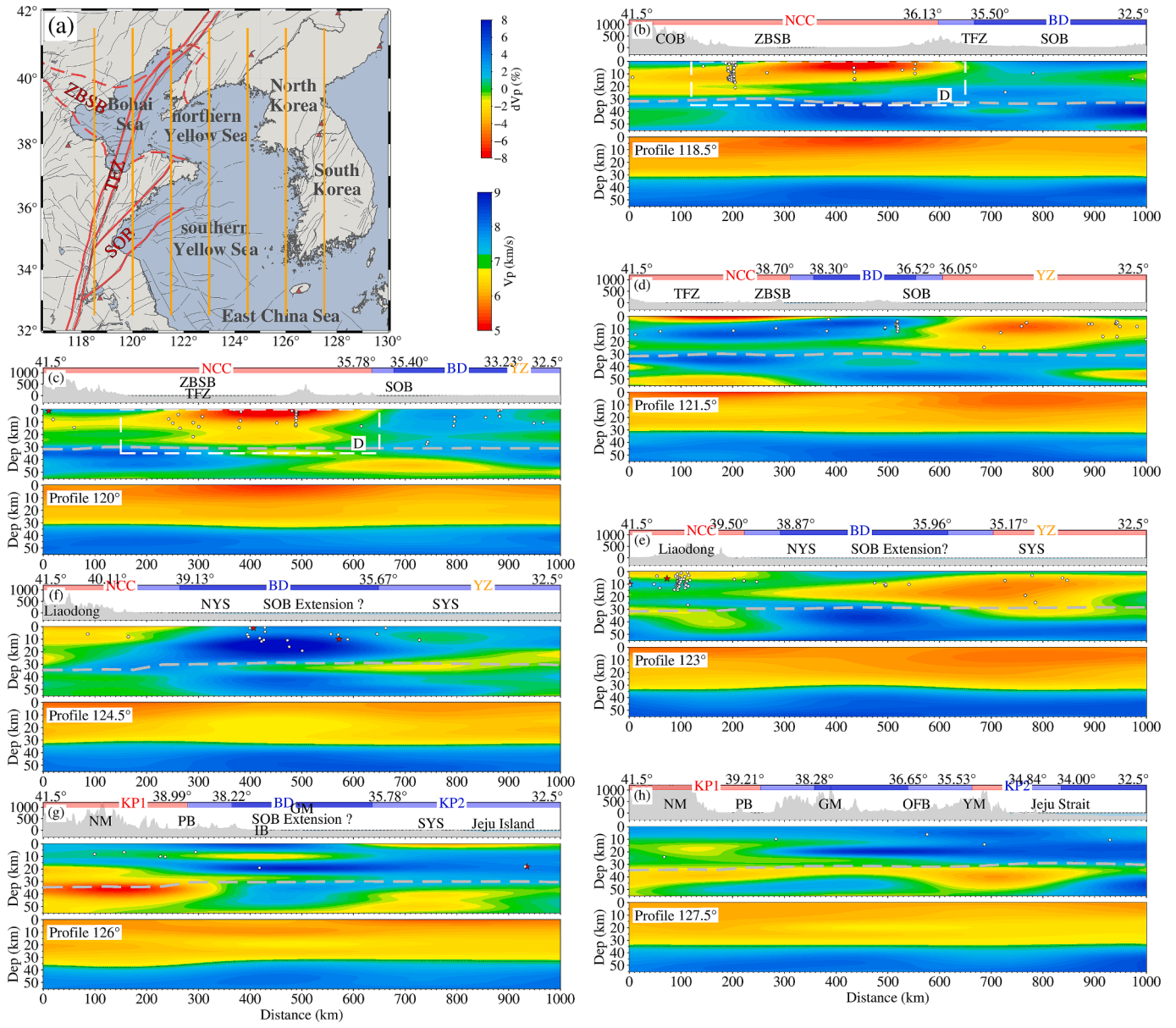

Fig. 9. Longitudinal profiles of relative and absolute velocities. Longitudinal profile locations are shown in (a). Each longitudinal profile includes the topography at the top, relative velocity in the middle, and absolute velocity at the bottom, with color bars provided. Panels (b) to (h) show profiles at 118.5°, 120°, 121.5°, 123°, 124.5°, 126°, and 127.5°, respectively. Profiles are divided into subregions based on relative velocity, with red (low) and blue (high) indicating anomaly strength from light (weak) to dark (strong) (see, Fig. S19). Geological units are labeled, including the North China Craton (NCC), northern Korean Peninsula (KP1), southern Korean Peninsula (KP2), high-velocity collision boundary (BD), and southern Yangtze Craton (YZ). The Moho is projected as a gray dashed line (Chang & Baag, 2007; Choi et al., 2015; Xu et al., 2016b; Zhang et al., 2019). Earthquakes of M_L 3.0 and above are marked with white stars, and historical ones of M_L 6.0 and above with red stars. (For interpretation of the references to colour in this figure legend, the reader is referred to the web version of this article.)

similar low-velocity zone is also observed in the Bohai region, as shown in the longitudinal profiles at 118.5° and 120° and the latitudinal profiles at 39° and 40° (Region D). However, the low-velocity anomalies in the Bohai region appear less laterally extensive compared to those in the Yellow Sea.

In the longitudinal profile at 127.5° (Fig. 9h), the southern part of the Korean Peninsula (south of ~37°) exhibits consistently high velocities, in contrast to the relatively lower velocities in the north. This north-south structural contrast has been noted in previous studies (Li et al., 2007; Hong & Kang, 2009), suggesting a possible structural boundary within the peninsula. High-velocity features observed beneath the Hongseong area, the Imjingang Belt, and the Sulu region appear structurally coherent at different depths, indicating that these regions may share a common tectonic origin related to the Triassic collision.

9. Tectonic implications

By mapping the subdivisions of the longitudinal and latitudinal profiles onto a plane, the northwestern segment of the Triassic collision boundary (BD) can be delineated as Line A in Fig. 11. Line A follows a consistent high–low velocity contrast observed in both horizontal and vertical sections, marking the boundary between the relatively low-velocity NCC and the high-velocity BD region. It generally coincides with the present-day trace of the Sulu Orogenic Belt (SOB), extending northwestward across the central Yellow Sea, into the northern Yellow Sea, and reaching the western coast of the Korean Peninsula (KP).

In the eastern part of the study area, our results suggest two possible structural boundaries. The southern Korean Peninsula exhibits prominent high-velocity anomalies, while lower velocities dominate the

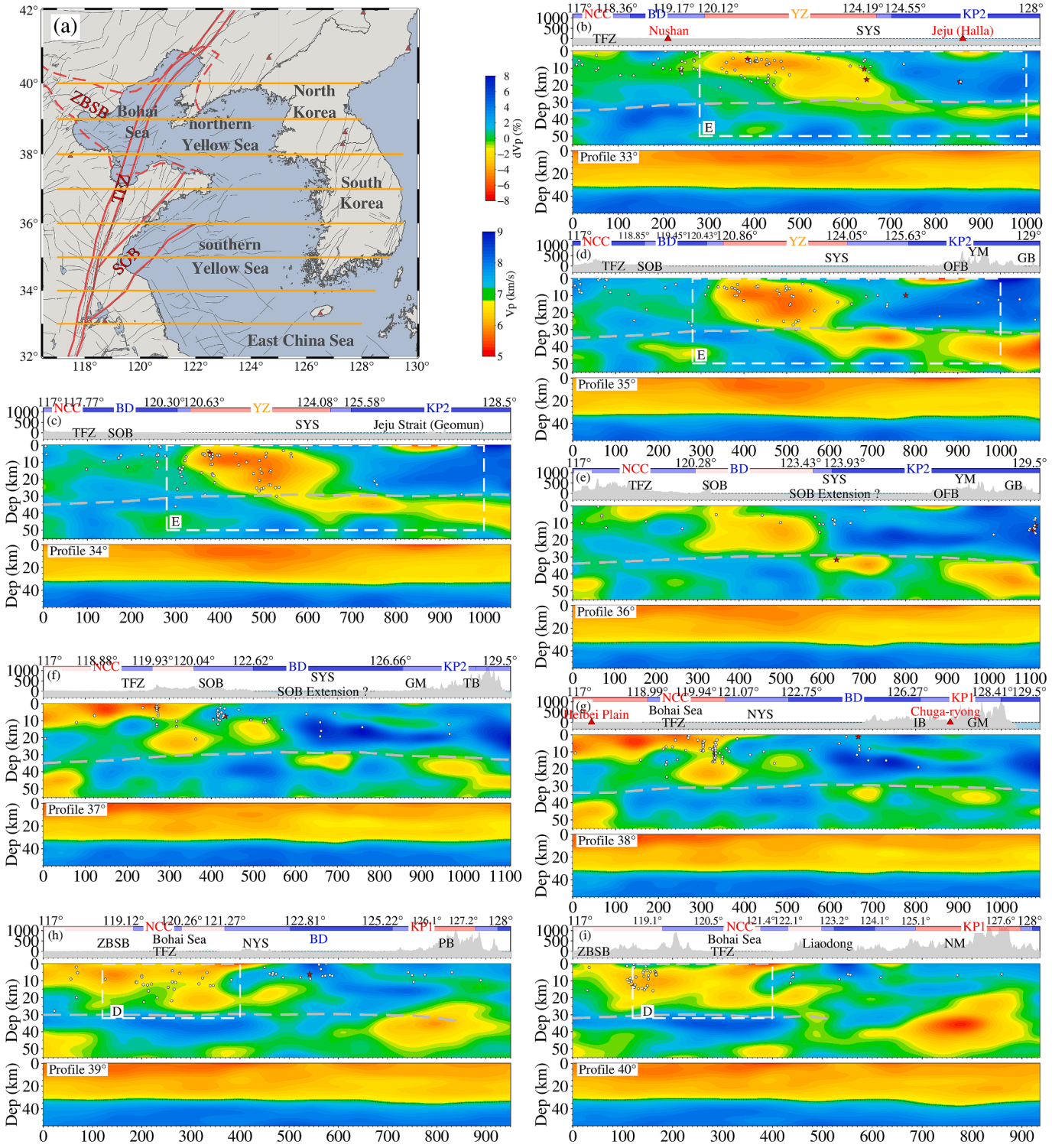

Fig. 10. Latitudinal profiles of relative and absolute velocities. Latitudinal profile locations are shown in (a). Each latitudinal profile includes the topography at the top, relative velocity in the middle, and absolute velocity at the bottom, with color bars provided. Panels (b) to (h) show profiles at 33°, 34°, 35°, 36°, 37°, 38°, 39°, and 40° respectively. Profiles are divided into subregions based on relative velocity, with red (low) and blue (high) indicating anomaly strength from light (weak) to dark (strong) (see, Fig. S20). Geological units are labeled, including the North China Craton (NCC), northern Korean Peninsula (KP1), southern Korean Peninsula (KP2), high-velocity collision boundary (BD), and southern Yangtze Craton (YZ). The Moho is projected as a gray dashed line (Chang & Baag, 2007; Choi et al., 2015; Xu et al., 2016b; Zhang et al., 2019). Earthquakes of M_L 3.0 and above are marked with white stars, and historical ones of M_L 6.0 and above with red stars. (For interpretation of the references to colour in this figure legend, the reader is referred to the web version of this article.)

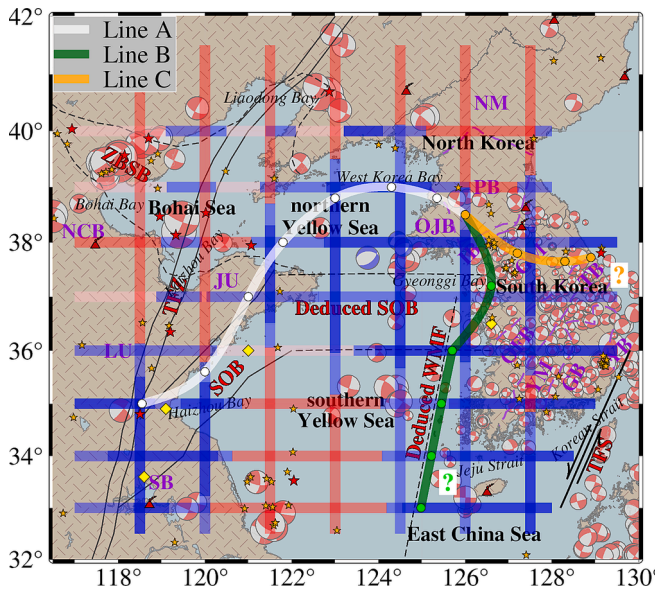

Fig. 11. The subdivisions of the region based on vertical velocity cross sections. The observed collision boundary is indicated (Line A), and two other possible structural boundaries are marked (Line B and Line C).

northern peninsula and the southern Yellow Sea. We assume that the high-velocity pattern in the KP appears somewhat different from that in the Sulu orogen: in the KP, the upper mantle shows relatively low velocities whereas the crust is characterized by high velocities, while in the Sulu region both the crust and mantle exhibit overall high velocities. The weak crustal low-velocity anomaly of the Sulu in the 36° profile could be related to the influence of Yellow Sea extension. Based on these contrasts, we delineate two candidate boundaries: Line B and Line C in Fig. 11. Line B traces the velocity contrast between the southern Yellow Sea and the southern Korean Peninsula. It branches off from Line A and internally includes the Ongjin Basin (OJB), Imjingang Belt (IB), and the Hongseong area in the Gyeonggi Massif (GM), which correspond to the strongest high-velocity zone observed in Profile 126°. The boundary then continues southeastward, roughly following the West Marginal Fault (WMF), and may indicate a strike-slip boundary developed during the Triassic collision. Both the WMF and the Tanlu Fault Zone (TFZ) coincide with zones of Moho depression in the latitudinal absolute velocity profiles, supporting the possibility that the WMF, like the TFZ, is a deep-penetrating structure formed during the collision. Line C, on the other hand, traces the contrast between the northern and southern Korean Peninsula. It also branches from Line A, beginning at the Ongjin Basin (OJB) and Imjingang Belt (IB), crossing the Gyeonggi Massif (GM), and reaching the Taebaeksan Basin (TB).

Seismic profiles and drilling results from the southern Yellow Sea show three fault types: reverse faults, strike-slip faults, and listric normal faults (Chang, 2015; Zou et al., 2016; Xu et al., 2019; Xuan et al., 2020; Zhang et al., 2021; Hu et al., 2022a; Zhang et al., 2022; Ma et al., 2023; Zhao et al., 2024). Abundant seismic profiles, rock samples, magmatic data, gravity data, and basin modeling confirm that magmatic activity occurred in this area due to basin extension after the collision (Lee et al., 2006; Hao et al., 2007; Li et al., 2009; Pang et al., 2017a; Pang et al., 2017b; Wang et al., 2017b; Hu et al., 2022b). The dominant stress field is suggested to have changed with tectonic evolution (Liang et al., 2003; Zhang et al., 2007; Li et al., 2016; Lei et al., 2018; Petrishchevsky, 2022). During the collision phase, convergence is the main force, forming thrust faults (Fig. 12b). After the collision, mantle upwelling led to extensive volcanic activity in the southern Yellow Sea. Divergence then became the dominant force, creating a widespread low-velocity zone (LVZ) that extends beneath the southwestern Korean Peninsula (Fig. 12c).

The inverted velocity models reveal the possible Triassic collision boundary between the YB and the SKC, along with basin extension features in the SYS. We infer the collision zone fully overlaps with the Sulu Orogenic Belt (SOB) and extends eastward into the Yellow Sea. It covers the potential extension zone of the SOB and continues to the western coast of the KP. This zone encompasses the Ongjin Basin and the western side of the Imjingang Belt, then curves southward through the Hongseong area. Based on the two possible structural boundaries, two potential models are proposed (Fig. 12a). The first model is based on the structural boundary that corresponds to the WMF. Velocity

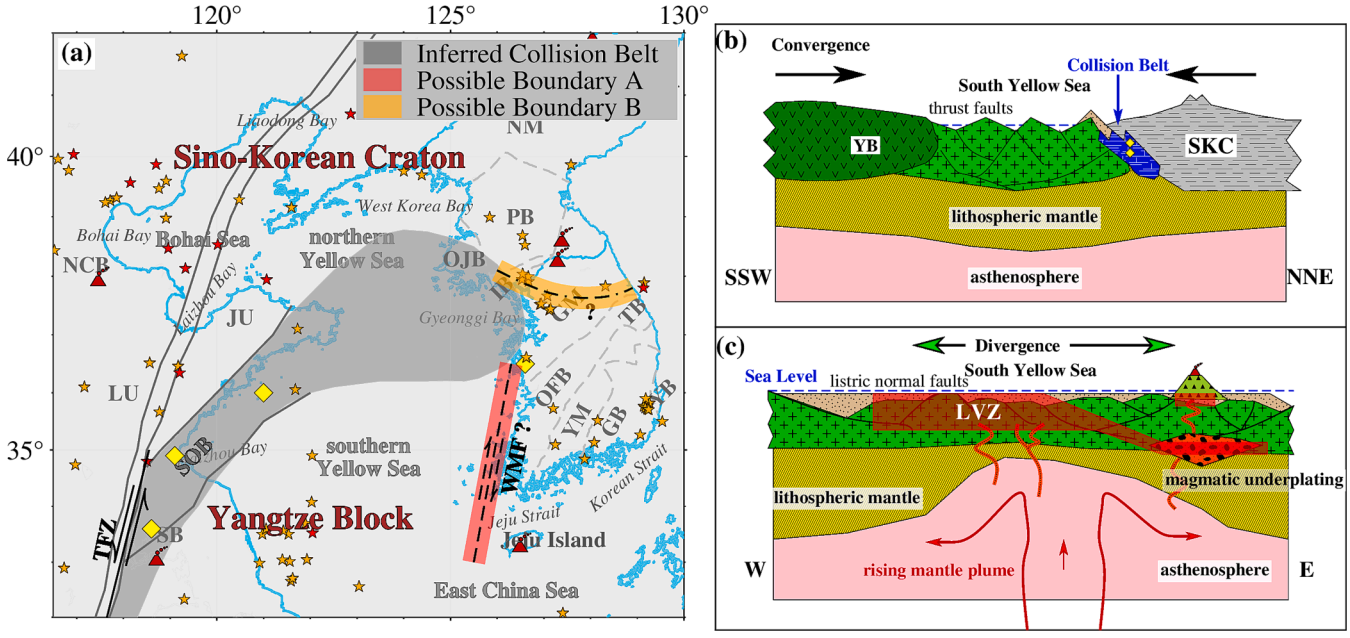

Fig. 12. Collision belt, structural boundaries, and schematic tectonic models: (a) One Possible Collision model. Inferred collision belt, possible structural boundary A (WMF) and possible structural boundary B are marked; (b) Schematic diagram of the NNE-oriented collision process in the southern Yellow Sea; (c) Schematic diagram of the WE-oriented extension in the southern Yellow Sea and the formation of the low-velocity zone (LVZ). (For interpretation of the references to colour in this figure legend, the reader is referred to the web version of this article.)

characteristics differ significantly between eastern and western regions. The second model focuses on the structural boundary crossing the middle of KP. Velocity characteristics sharply contrast between northern and southern regions. The first model suggests that, during the Triassic collision, the entire KP belong to the SKC. The second model implies the northern KP was part of the SKC, while the southern KP corresponded to the YB.

9.1. Sulu orogenic belt extension across the Yellow Sea

The Sulu Orogenic Belt (SOB) is widely recognized as the collision boundary between the Yangtze Block and the North China Craton (Xu et al., 2021; Hu et al., 2022a). Along the SOB, several eclogite samples have been reported in prior studies (Li et al., 2000; Zhang et al., 2009), with the westernmost sample found on Qialiyan Island, near the central Yellow Sea (Li et al., 2014). These eclogites represent exhumed fragments of a subducted paleo-oceanic plate, likely formed during the Yangtze–North China collision (Ye et al., 2021; Luo et al., 2022). Seismic studies have shown that the SOB is characterized by high-velocity anomalies, a typical feature of collision fronts (Xu, 2001; Bai et al., 2007; Luo et al., 2022).

The possible offshore continuation of the SOB into the Yellow Sea has long been proposed (Ree et al., 1996). Our results indicate that this extension is significantly broader than previously recognized, with its northern margin reaching the northern Yellow Sea. Some studies based on seismic profiles, well data, magnetic reversal data, and field observations also suggest that the extension of the SOB is likely significantly wider than previously thought and extends to Yellow Sea (Hu et al., 2022a). Focal-mechanism solutions show predominantly strike-slip events in the central Yellow Sea, along with ENE–WSW-oriented normal faults that appear to mark the northern boundary of the collision. This structural pattern suggests that the SOB extends across the Yellow Sea and may reach toward the western coast of the Korean Peninsula (Hong & Choi, 2012). In addition, crustal density modeling based on TRIDENT satellite gravity data reveals a high-gravity anomaly from the Sulu Belt into the Yellow Sea, closely matching the high-velocity collision zone identified in this study (Choi et al., 2015).

The SOB also appears to extend into the Korean Peninsula through connections with major tectonic belts. The Imjingang Belt has been considered a possible segment of the collision zone due to its deformation and metamorphism during the same collisional event (Chough et al., 2000). Genetic links between the Imjingang and Sulu belts are supported by similarities in age, metamorphic characteristics, and post-orogenic magmatism (Cho et al., 2008). Furthermore, the collision belt inferred in our study passes through the Hongseong area, where high-pressure and high-temperature eclogites comparable to those in the SOB have been identified (Oh et al., 2005). Isotopic dating confirms a shared origin for the Hongseong and Sulu eclogites (Zhai et al., 2007), and interpretations of GRACE satellite gravity data suggest that both the Imjingang Belt and the Hongseong area form the eastern margin of the collision structure (Choi et al., 2006).

9.2. Eastern structural boundaries and possibilities of South China rotation

Our results infer two possible eastern structural boundaries: one is the West Marginal Fault (WMF) in the Yellow Sea, and the other is a boundary located in the Korean Peninsula (KP).

The WMF might represent a potential structural boundary. We find the west and east sides of the west marginal fault (WMF) exhibit different characteristics. The WMF region shows predominantly high velocities, with structural features that slightly differ from those of the Sulu Belt and its extensions. This suggests that the WMF may exist. Recent seismic profile studies have confirmed the existence of the WMF and identified its location, describing it as a typical strike-slip fault with reverse-faulting characteristics (Zhang et al., 2022; Zhao et al., 2024). Comprehensive analysis of geological and geophysical data from China's marginal seas revealed the WMF could serve as a strike-slip boundary (Hao et al., 2002; Hou et al., 2022). Some models suggest the Yangtze Block (YB) was embedded within the South Korean Craton (SKC) to the north, with the Tanlu Fault Zone (TFZ) forming the western boundary, the WMF serves as the eastern boundary, the WMF exhibits both strike-slip and reverse faulting characteristics potentially resulting from the rotation of the Yangtze Block (Hao et al., 2007; Zhai et al., 2007; Chang & Zhao, 2012; Chang, 2015).

A second possible eastern boundary is suggested by a significant velocity structure difference between the northern and southern KP. This boundary starts at the Ongjin Basin (OJB) and Imjingang Belt (IB), passes through the Gyeonggi Massif (GM), and reaches the Taebaeksan Basin (TB). Teleseismic traveltime tomography, local traveltime tomography, ambient noise tomography, and attenuation tomography from previous studies confirm this difference (Hong, 2010; Kim et al., 2017a; Wang et al., 2017a; Song et al., 2020). Petrographic studies suggest that the collision initially occurred in the eastern part of the South China Block (KP), and later in the Dabie–Sulu Orogenic Belt. During this process, relative clockwise rotation occurred between the Sino–Korean Craton and South China Block (Zhang, 1997; Oh, 2006). So the boundary in KP may be the position of initial collision, later the collision progressing to the Dabie–Sulu Orogenic Belt, possibly accompanied by rotation of the South China Block.

Additionally, the collision belt broadens significantly from the central Yellow Sea to the western coast of the Korean Peninsula, potentially due to rotation. Several paleomagnetic studies suggest that the Yangtze Block, or South China Block, experienced significant rotation of 30° to 70° relative to the South Korean Craton (Gilder et al., 1999; Zhao et al., 1999; Huang et al., 2018; Peng et al., 2022). Some collision models effectively incorporate the rotation of the South China Block, suggesting that the rotation of the Yangtze Block led to subsequent thrust along the WMF, supporting the idea that the initial collision likely aligned with a NNE orientation, consistent with the strikes of both the Tanlu Fault and WMF (Chang & Zhao, 2012; Hu et al., 2022a). Thus, the rotation of the South China Block may have occurred during the collision.

9.3. Basin formation in the southern Yellow Sea

A broad low-velocity anomaly extends from the southern Yellow Sea to the southern Korean Peninsula, corresponding to widespread low velocities in the upper and middle crust along profiles 123°–126° and 33°–36°. This anomaly likely reflects basin-wide crustal thinning and magmatic activity. Multichannel seismic surveys have imaged abundant igneous features—including stocks, laccoliths, sills, dikes, and hydrothermal vent systems—formed during basin extension (Lee et al., 2006). Interpretation of 2-D marine seismic profiles further reveals the coexistence of normal, thrust, and strike-slip faults in the southern Yellow Sea, indicating a tectonic transition from compression to extension (Zhang et al., 2021).

The East Block (EB) experienced multiple extensional episodes during the late Mesozoic and Cenozoic (Ren et al., 2002; Kusky et al., 2007; Lin & Wei, 2020). Seismic profile data indicate three major deformation stages since the Indosinian orogeny: an initial foreland compression stage, a transitional phase, and the development of a Neogene–Quaternary depression associated with Late Cretaceous–Paleogene drifting (Lei et al., 2018). Such tectonic evolution likely facilitated the observed crustal extension and its associated low-velocity structure. Comparable low-velocity anomalies in the EB have been linked to lithospheric upwelling, as indicated by ambient noise, surface-wave, and anisotropic tomography (Tian & Zhao, 2013; Chen et al., 2014; Ma et al., 2022), as well as receiver-function and seismic-imaging studies (He, 2020; Liu et al., 2022). Additional supporting evidence includes the occurrence of Mesozoic–Cenozoic mantle peridotites (Liu et al., 2019; Zhao et al., 2023) and dome-like crustal structures in the EB and southern Yellow Sea Basin (Jia et al., 2014; Ma et al., 2023;

Zhao et al., 2023). These results collectively indicate that the southern Yellow Sea Basin has undergone substantial extension and may still be actively deforming.

10. Discussion and conclusions

We conducted P-wave traveltime tomography across the eastern Sino–Korean Craton using dense seismic networks in both China and Korea. The inverted velocity model in the region reveals information about the Triassic collision and basin extension, refining structural boundaries and features related to these tectonic processes. The velocity results show relatively low-velocity anomalies in the North China Craton, the southern Yellow Sea, and the northern Korean Peninsula, contrasting with high-velocity zones in the southern Korean Peninsula and the Sulu Orogenic Belt.

We identify three principal boundaries in the study area. The first is a well-constrained collision boundary exhibiting a sharp velocity contrast: low velocities correspond to the North China Craton on one side, while comparatively higher velocities are associated with the collision belt on the other. The southern portion of this boundary coincides with the Sulu Orogenic Belt. Afterward, it extends eastward into the northern Yellow Sea and further reaches the western coast of the Korean Peninsula. In addition to this collision boundary, two significant structural boundaries marked by pronounced velocity contrasts are recognized. One is located in the southern Yellow Sea near the western Korean Peninsula and may correspond to the West Marginal Fault. The other traverses the Korean Peninsula, originating at the Ongjin Basin and the Imjingang Belt, passing through the Gyeonggi Massif, and extending to the Taebaeksan Basin. Based on these boundaries, two tectonic models are proposed for the Triassic collision period: one suggests that the entire Korean Peninsula is part of the Sino-Korean Craton, while the other argues that only the northern peninsula belongs to it.

We also identify a prominent low-velocity zone extending from the crust of the southern Yellow Sea to the mantle beneath the southern Korean Peninsula. This feature may be attributed to basin spreading and mantle upwelling, although the timing of this extension is unclear. Convergence during the collision likely caused thrust faulting in the southern Yellow Sea. Subsequently, mantle upwelling and extensional divergence may have driven the formation of listric normal faults and contributed to the development of the low-velocity zone.

Several limitations of this study should be acknowledged. Minor uncertainties may arise from factors such as origin-time errors and picking errors, although their impact is expected to be small. The reliance on P-wave data may not capture all relevant tectonic processes. The velocity structure does not reveal the direction of tectonic movements or rotation, limiting the interpretation of geodynamic processes. The spatial resolution may not be sufficient to detect smaller-scale features, such as confirming the West Marginal Fault. The shape of the collision zone may curve southeast in the central Yellow Sea, potentially due to South China Block rotation, though the extent of the rotation remains uncertain. The extensive low-velocity zone in the southern Yellow Sea likely results from basin extension, though other causes cannot be ruled out. Although the Moho beneath the region does not show significant topographic variation (generally within ~3 km), we cannot completely exclude the potential influence of crustal thickening on the observed low-velocity anomalies. Since the anomalies extend across the Moho into the upper mantle, additional mantle-scale processes such as partial melting or lithospheric modification may also be involved. The relatively thick sedimentary cover beneath the southwestern Yellow Sea near the China continent, as suggested by the GlobSed model, could contribute to a slight overestimation of the lateral or vertical extent of the low-velocity anomaly (Straume et al., 2019).

However, this study benefits from the inclusion of data from a comprehensive network of stations across both China and Korea. The dense ray coverage in the study area and the high quality local traveltime data provide strong constraints on the crust-to-upper mantle structure. This approach allows for more precise identification of key tectonic features, such as the potential location of the West Marginal Fault and the clear delineation of the velocity contrast boundary between the northern and southern Korean Peninsula. Furthermore, we can clearly observe the Sulu collision belt stretching into the Yellow Sea and further toward the west coast of the Korean Peninsula, validating the hypothesis proposed by several studies regarding the Sulu belt. Additionally, the low-velocity zone extending from the southern Yellow Sea to the Korean Peninsula is clearly visible, a feature not previously observed in earlier studies. Future research could incorporate tomography results from other seismic phases and integrate additional methods, such as geodetic and geological studies, along with anisotropic analyses, to further enhance the understanding of the region's complex tectonic evolution.

CRediT authorship contribution statement

Yanbing Liu: Writing – original draft, Visualization, Validation, Software, Methodology, Investigation, Formal analysis, Data curation, Conceptualization. **Tae-Kyung Hong:** Writing – review & editing, Supervision, Resources, Project administration, Funding acquisition, Conceptualization. **Junhyung Lee:** Funding acquisition, Data curation. **Seongjun Park:** Supervision, Funding acquisition, Conceptualization. **Samuel Celis:** Validation, Investigation, Conceptualization. **Yuxuan Chen:** Validation, Data curation. **Jeongin Lee:** Software, Data curation. **Byeongwoo Kim:** Software, Data curation.

Declaration of competing interest

The authors declare that they have no known competing financial interests or personal relationships that could have appeared to influence the work reported in this paper.

Acknowledgement

We sincerely thank Dr. Nick Rawlinson and an anonymous reviewer for their constructive comments, which greatly improved the quality of this manuscript and helped correct several errors. We acknowledge the China Earthquake Disaster Prevention Center for fault data; the China Earthquake Networks Center and Beijing Earthquake Agency for traveltime data, historical major event catalogs, and focal mechanism solutions; and the Korea Meteorological Administration for waveform data and historical major event catalogs. Most figures are generated using Generic Mapping Tools (Wessel et al., 2019). This work is supported by the Korea Meteorological Administration Research and Development Program under grant KMI2022-00710. Additionally, this research is partly supported by the Basic Science Research Program of National Research Foundation of Korea (RS-2025-23963785) and the Young Elite Scientist Sponsorship Program of Beijing Association for Science and Technology (No. BYESS2023029).

Appendix A. Supplementary data

Supplementary data to this article can be found online at https://doi.org/10.1016/j.gr.2025.11.006.

References

Bai, Z.M., Zhang, Z.J., Wang, Y.H., 2007. Crustal structure across the Dabie-Sulu orogenic belt revealed by seismic velocity profiles. J. Geophys. Eng. 4, 436–442. https://doi.org/10.1088/1742-2132/4/4/009.

Brenna, M., Cronin, S.J., Kereszturi, G., Sohn, Y.K., Smith, I.E.M., Wijbrans, J., 2015. Intraplate volcanism influenced by distal subduction tectonics at Jeju Island, Republic of Korea. Bull. Volcanol. 77, 7. https://doi.org/10.1007/s00445-014-0896-5.

Chang, K.-H., Park, S.-O., 2001. Paleozoic Yellow Sea Transform Fault: its Role in the Tectonic history of Korea and Adjacent Regions. Gondwana Res. 4, 588–589. https://doi.org/10.1016/s1342-937x(05)70393-2.

Chang, K.-H., Zhao, X., 2012. North and South China suturing in the east end: what happened in Korean Peninsula? Gondwana Res. 22, 493–506. https://doi.org/10.1016/j.gr.2011.12.010.
Chang, K.-H., 2015. Yellow Sea Transform Fault (YSTF) and the development of Korean Peninsula. Russ. J. Pac. Geol. 9, 81–95. https://doi.org/10.1134/S1819714015020037.
Chang, S.J., Baag, C.E., 2007. Moho Depth and Crustal VP/VS Variation in Southern Korea from Teleseismic Receiver Functions: Implication for Tectonic Affinity between the Korean Peninsula and China. Bull. Seismol. Soc. Am. 97, 1621–1631. https://doi.org/10.1785/0120050264.
Chen, B., Zhai, M.-G., Tian, W., 2007. Origin of the Mesozoic magmatism in the North China Craton: constraints from petrological and geochemical data, In: Zhai, M.-G., Windley, B.F., Kusky, T.M. and Meng, Q.R. (Eds.), Mesozoic Sub-Continental Lithospheric Thinning under Eastern Asia. Geological Society, London, Special Publications, 280, pp. 131–151. Doi: 10.1144/SP280.6.
Chen, H.P., Zhu, L.B., Wang, Q.D., Zhang, P., Yang, Y.H., 2014. S-wave velocity structure of the North China from inversion of Rayleigh wave phase velocity. J. Asian Earth Sci. 88, 178–191. https://doi.org/10.1016/j.jseaes.2014.03.006.
Chen, L., Zheng, T.Y., Xu, W.W., 2006. A thinned lithospheric image of the Tanlu Fault Zone, eastern China: Constructed from wave equation based receiver function migration. J. Geophys. Res. Solid Earth 111, B09312. https://doi.org/10.1029/2005JB003974.
Chen, Y.X., Zheng, Y.F., 2013. Petrological evidence for crustal anatexis during continental collision in the Sulu orogen. Chin. Sci. Bull. 58, 2198–2202. https://doi.org/10.1360/csb2013-58-22-2198 (in Chinese).
Cheong, C.-S.A., Jo, H.J., Jeong, Y.J., Li, X.H., 2018. Magmatic response to the interplay of collisional and accretionary orogenies in the Korean Peninsula: Geochronological, geochemical, and O-Hf isotopic perspectives from Triassic plutons. Geol. Soc. Am. Bull. 131, 609–634. https://doi.org/10.1130/b32021.1.
Cheong, C.S., Kee, W.S., Jeong, Y.J., Jeong, G.Y., 2006. Multiple deformations along the Honam shear zone in southwestern Korea constrained by Rb-Sr dating of synkinematic fabrics: Implications for the Mesozoic tectonic evolution of northeastern Asia. Lithos 87, 289–299. https://doi.org/10.1016/j.lithos.2005.06.015.
Cho, D.L., Lee, S.R., Armstrong, R., 2008. Termination of the Permo-Triassic Songrim (Indosinian) orogeny in the Ogcheon belt, South Korea: Occurrence of ca. 220 Ma post-orogenic alkali granites and their tectonic implications. Lithos 105, 191–200. https://doi.org/10.1016/j.lithos.2008.03.007.
Choi, D., 2014. Geology and Tectonic Evolution of the Korean Peninsula. Seoul National University Press, Seoul (in Korean), 277 p.
Choi, D.K., Woo, J., Park, T.Y., 2012. The Okcheon Supergroup in the Lake Chungju area, Korea: Neoproterozoic volcanic and glaciogenic sedimentary successions in a rift basin. Geosci. J. 16, 229–252. https://doi.org/10.1007/s12303-012-0031-6.
Choi, S., Oh, C.-W., Luehr, H., 2006. Tectonic relation between northeastern China and the Korean peninsula revealed by interpretation of GRACE satellite gravity data. Gondwana Res. 9, 62–67. https://doi.org/10.1016/j.gr.2005.06.002.
Choi, S., Ryu, I.C., Götze, H.J., 2015. Depth distribution of the sedimentary basin and Moho undulation in the Yellow Sea, NE Asia interpreted by using satellite-derived gravity field. Geophys. J. Int. 202, 41–53. https://doi.org/10.1093/gji/ggv108.
Chough, S.K., Kwon, S.T., Ree, J.H., Choi, D.K., 2000. Tectonic and sedimentary evolution of the Korean peninsula: a review and new view. Earth Sci. Rev. 52, 175–235. https://doi.org/10.1016/S0012-8252(00)00029-5.
Chough, S.K., Shinn, Y.J., Yoon, S.H., 2018. Regional strike-slip and initial subsidence of Korea Plateau, East Sea: tectonic implications for the opening of back-arc basins. Geosci. J. 22, 533–547. https://doi.org/10.1007/s12303-018-0017-0.
Crosson, R.S., 1976. Crustal structure modeling of earthquake data: 1. Simultaneous least squares estimation of hypocenter and velocity parameters. J. Geophys. Res. 81, 3036–3046. https://doi.org/10.1029/JB081i017p03036.
Efron, B., Tibshirani, R., 1991. Statistical data analysis in the computer age. Science 253, 390–395. https://doi.org/10.1126/science.253.5018.390.
Fang, L.H., Wu, J.P., Wang, W.L., Wang, C.Z., Yang, T., 2013. Love wave tomography from ambient seismic noise in North-China. Chin. J. Geophys. 56, 2268–2279. https://doi.org/10.6038/cjg20130714 (in Chinese).
Feng, J.K., Yao, H.J., Chen, L., Li, C.L., 2022. Ongoing Lithospheric alteration of the north china craton revealed by surface-wave tomography and geodetic observations. Geophys. Res. Lett. 49, e2022GL099403. https://doi.org/10.1029/2022GL099403.
Ge, C., Zheng, Y., Xiong, X., 2011. Study of crustal thickness and Poisson ratio of the North China Craton. Chin. J. Geophys. 54, 2538–2548. https://doi.org/10.3969/j.issn.0001-5733.2011.10.011 (in Chinese).
Gilder, S.A., Leloup, P.H., Courtillot, V., Chen, Y., Coe, R.S., Zhao, X.X., Xiao, W.J., Halim, N., Cogné, J.P., Zhu, R.X., 1999. Tectonic evolution of the Tancheng-Lujiang (Tan-Lu) fault via Middle Triassic to Early Cenozoic paleomagnetic data. J. Geophys. Res. Solid Earth 104, 15365–15390. https://doi.org/10.1029/1999JB900123.
Griffin, W.L., Andi, Z., O'Reilly, S.Y., Ryan, C.G., 1998. Phanerozoic evolution of the lithosphere beneath the Sino-Korean Craton, In: Flower, M.F.J., Chung, S.-L., Lo, C.-H. and Lee, T.-Y. (Eds.), Mantle Dynamics and Plate Interactions in East Asia. American Geophysical Union, Washington, DC, pp. 107–126. Doi: 10.1029/GD027p0107.
Gu, G.X., 1983. Catalogue of Chinese Earthquakes, 1831 B.C.–1969 A.D. Science Press, Beijing (in Chinese), 872 p.
Hacker, B.R., Ratschbacher, L., Liou, J.G., 2004. Subduction, collision and exhumation in the ultrahigh-pressure Qinling-Dabie orogen, In: Malpas, J., Fletcher, C.J.N., Ali, J.R. and Aitchison, J.C. (Eds.), Aspects of the Tectonic Evolution of China. Geological Society, London, Special Publications, 226, pp. 157–175. Doi: 10.1144/GSL.SP.2004.226.01.09.
Han, S.C., Zhang, H.J., Xin, H.L., Shen, W.S., Yao, H.J., 2021. USTClitho2.0: Updated Unified Seismic Tomography Models for Continental China Lithosphere from Joint Inversion of Body-Wave Arrival Times and Surface-Wave Dispersion Data. Seismol. Res. Lett. 93, 201–215. https://doi.org/10.1785/0220210122.
Hao, A.W., Zhang, H.J., Han, S.C., Maceira, M., 2023. High-resolution lithospheric structure of continental China from joint inversion of surface wave and gravity data. Tectonophysics 868. https://doi.org/10.1016/j.tecto.2023.230079.
Hao, T.Y., Suh, M., Wang, Q.S., Choi, S., Jiang, W.W., Song, H.B., Yan, X.W., Liu, J.H., Yao, C.L., 2002. A study on the extension of fault zones in Yellow Sea and its adjacent areas based on gravity data. Chin. J. Geophys. 45, 385–397. https://doi.org/10.1002/cjg2.252.
Hao, T.Y., Xu, Y., Suh, M., Xu, Y., Liu, J.H., Zhang, L.L., Dai, M.G., 2007. East Marginal Fault of the Yellow Sea: a part of the conjunction zone between Sino-Korea and Yangtze Blocks? Geol. Soc. Spec. Publ. 280, 281–291. https://doi.org/10.1144/SP280.14.
Hao, T.Y., Liu, J.H., Suh, M., Choi, S., Yan, X.W., Liu, Z.F., 2013. Deep structure characteristics and geological evolution in yellow sea and adjacent region. Chin. J. Geophys. 46, 1148–1156. https://doi.org/10.1002/cjg2.434.
He, C.S., 2020. Upwelling mantle plume and lithospheric delamination beneath the North China Craton. Phys. Earth Planet. Inter. 306. https://doi.org/10.1016/j.pepi.2020.106548.
Hong, T.K., Menke, W., 2008. Imaging laterally varying regional heterogeneities from seismic coda using a source-array analysis. Phys. Earth Planet. Inter. 166, 188–202. https://doi.org/10.1016/j.pepi.2008.01.001.
Hong, T.K., Kang, T.S., 2009. Travel-time tomography of the paleo-continental-collision and rifting zone around Korea and Japan. Bull. Seismol. Soc. Am. 99, 416–421. https://doi.org/10.1785/0120080120.
Hong, T.K., 2010. Attenuation in a region with both continental and oceanic environments. Bull. Seismol. Soc. Am. 100, 851–858. https://doi.org/10.1785/0120090057.
Hong, T.K., Choi, H., 2012. Seismological constraints on the collision belt between the North and South China blocks in the Yellow Sea. Tectonophysics 570, 102–113. https://doi.org/10.1016/j.tecto.2012.08.034.
Hong, T.K., Park, S., Lee, J., Lee, J., Kim, B., 2024. Middle to lower crustal earthquakes in the western East Sea (Sea of Japan) and their implications for neotectonic evolution. Tectonophysics 880. https://doi.org/10.1016/j.tecto.2024.230346.
Hou, F.H., Zhu, X.Q., Zhang, X.H., Wu, Z.Q., Guo, X.W., Qi, J.H., Wen, Z.H., Wang, B.J., Meng, X.J., 2022. Basic geological characteristics of the East China Sea region and geological-geophysical characterization of some important tectonic boundaries in the region. Earth Sci. Front. 29, 281–293. https://doi.org/10.13745/j.esf.sf.2021.10.37.
Hu, P.P., Yang, F.L., Li, S.Z., Zhang, R.Y., Ni, B., Qiu, E.R., Suo, Y.H., 2022a. Opposite thrust systems under the Subei-South Yellow Sea Basin: a synthesis on the closure of the eastern Tethyan Ocean. Earth Sci. Rev. 231. https://doi.org/10.1016/j.earscirev.2022.104075.
Hu, P.P., Yang, X.D., Yang, F.L., Zhang, J.C., Zhou, Z.Y., Dong, R.W., 2022b. Seismogenic Structure and Tectonic Mechanism of the 2021 Mw 5.0 Yancheng Earthquake in the South Yellow Sea Basin, East Asia. Seismol. Res. Lett. 94, 646–670. https://doi.org/10.1785/0220220163.
Huang, B.C., Yan, Y.G., Piper, J.D.A., Zhang, D.H., Yi, Z.Y., Yu, S., Zhou, T.H., 2018. Paleomagnetic constraints on the paleogeography of the East Asian blocks during late Paleozoic and Early Mesozoic times. Earth Sci. Rev. 186, 8–36. https://doi.org/10.1016/j.earscirev.2018.02.004.
Huang, W., Gao, W., Ding, G., 1996. Neogene volcanism and Holocene earthquakes in the Tanlu fault zone, eastern China. Tectonophysics 260, 259–270. https://doi.org/10.1016/0040-1951(95)00195-6.
Huang, X., Wang, W.T., Ding, Z.F., 2023. Sedimentary and crustal structure of eastern North China from joint inversion of Rayleigh wave phase velocity and ellipticity and its implication for magmatism. Tectonophysics 846. https://doi.org/10.1016/j.tecto.2022.229680.
Jia, S.X., Wang, F.Y., Tian, X.F., Duan, Y.H., Zhang, J.S., Liu, B.F., Lin, J.Y., 2014. Crustal structure and tectonic study of North China Craton from a long deep seismic sounding profile. Tectonophysics 627, 48–56. https://doi.org/10.1016/j.tecto.2014.04.013.
Jiang, G.Z., Hu, S.B., Shi, Y.Z., Zhang, C., Wang, Z.T., Hu, D., 2019. Terrestrial heat flow of continental China: updated dataset and tectonic implications. Tectonophysics 753, 36–48. https://doi.org/10.1016/j.tecto.2019.01.006.
Kennett, B.L.N., Engdahl, E.R., 1991. Traveltimes for Global Earthquake Location and phase Identification. Geophys. J. Int. 105, 429–465. https://doi.org/10.1111/j.1365-246X.1991.tb06724.x.
Kim, H.J., Kim, C.H., Ha, T.Y., Liu, L.H., Kim, K.H., Jun, H., Jou, H.T., Moon, S., Xue, Y., Wu, Z.Q., Lu, C.C., Lee, S.H., 2019. Crustal structure of the Gunsan Basin in the SE Yellow Sea from ocean bottom seismometer (OBS) data and its linkage to the South China Block. J. Asian Earth Sci. 180. https://doi.org/10.1016/j.jseaes.2019.103881.
Kim, K.H., Park, J.H., Park, Y., Hao, T.Y., Kim, H.J., 2017a. Crustal structure beneath the southern Korean Peninsula from local earthquakes. Geophys. J. Int. 209, 969–978. https://doi.org/10.1093/gji/ggx079.
Kim, S.W., Kwon, S., Ryu, I.C., 2009. Geochronological constraints on multiple deformations of the Honam Shear Zone, South Korea and its tectonic implication. Gondwana Res. 16, 82–89. https://doi.org/10.1016/j.gr.2008.12.004.
Kim, S.W., Kwon, S., Ryu, I.C., Jeong, Y.J., Choi, S.J., Kee, W.S., Yi, K., Lee, Y.S., Kim, B.C., Park, D.W., 2012. Characteristics of the early cretaceous igneous activity in the Korean peninsula and tectonic implications. J. Geol. 120, 625–646. https://doi.org/10.1086/667811.
Kim, S.W., Kwon, S., Park, S.I., Yi, K., Santosh, M., Kim, H.S., 2017b. Early to Middle Paleozoic tectonometamorphic evolution of the Hongseong area, central western

Korean Peninsula: Tectonic implications. Gondwana Res. 47, 308–322. https://doi.org/10.1016/j.gr.2016.05.016.
Kissling, E., 1988. Geotomography with local Earthquake Data. Rev. Geophys. 26, 659–698. https://doi.org/10.1029/RG026i004p00659.
Kissling, E., Lahr, J.C., 1991. Tomographic image of the Pacific Slab under Southern Alaska. Eclogae Geol. Helv. 84, 297–315.
Kissling, E., Ellsworth, W.L., Eberhartphillips, D., Kradolfer, U., 1994. Initial reference models in local earthquake tomography. J. Geophys. Res. Solid Earth 99, 19635–19646. https://doi.org/10.1029/93JB03138.
KMA, 2012. Historical Earthquake Records in Korea (2~1904). Korea Meteorological Administration, Seoul (in Korean), 279 p.
Kusky, T.M., Li, J.H., 2003. Paleoproterozoic tectonic evolution of the North China Craton. J. Asian Earth Sci. 22, 383–397. https://doi.org/10.1016/S1367-9120(03)00071-3.
Kusky, T.M., Windley, B.F., Zhai, M.G., 2007. Tectonic evolution of the North China Block: from orogen to craton to orogen. Geol. Soc. Spec. Publ. 280, 1–34. https://doi.org/10.1144/SP280.1.
Kusky, T.M., 2011. Geophysical and geological tests of tectonic models of the North China Craton. Gondwana Res. 20, 26–35. https://doi.org/10.1016/j.gr.2011.01.004.
Kusky, T.M., Polat, A., Windley, B.F., Burke, K.C., Dewey, J.F., Kidd, W.S.F., Maruyama, S., Wang, J.P., Deng, H., Wang, Z.S., Wang, C., Fu, D., Li, X.W., Peng, H.T., 2016. Insights into the tectonic evolution of the North China Craton through comparative tectonic analysis: a record of outward growth of Precambrian continents. Earth Sci. Rev. 162, 387–432. https://doi.org/10.1016/j.earscirev.2016.09.002.
Lamarre, M., Townshend, B., Shah, H.C., 1992. Application of the bootstrap method to quantify uncertainty in seismic hazard estimates. Bull. Seismol. Soc. Am. 82, 104–119. https://doi.org/10.1785/bssa0820010104.
Laske, G., Masters, G., Ma, Z., Pasyanos, M.E., 2013. Update on CRUST1.0 – A 1-degree global model of Earth's crust. EGU General Assembly Conference Abstracts 15.
Lee, B.C., Kim, S.W., Lee, B.Y., Oh, C.W., Cho, D.L., Kee, W.S., 2024. Middle Paleozoic metamorphic and sedimentary events in the central Korean Peninsula and their geological implications. Geosci. Front. 15. https://doi.org/10.1016/j.gsf.2024.101840.
Lee, D.S., 1987. Geology of Korea. Kyohak-Sa Publishing Co. and Geological Society of Korea, Seoul (in Korean), 514 p.
Lee, G.H., Kwon, Y.I., Yoon, C.S., Kim, H.J., Yoo, H.S., 2006. Igneous complexes in the eastern Northern South Yellow Sea Basin and their implications for hydrocarbon systems. Mar. Pet. Geol. 23, 631–645. https://doi.org/10.1016/j.marpetgeo.2006.06.001.
Lee, J.H., Oh, M.K., Choi, T., 2021. Recognition of the "Great Unconformity" in the eastern Sino-Korean Block: Insights from the Taebaek Group. Korea. Precambrian Res. 364. https://doi.org/10.1016/j.precamres.2021.106363.
Lee, K., Kim, J.K., 2002. Intensity attenuation in the Sino-Korean craton. Bull. Seismol. Soc. Am. 92, 783–793. https://doi.org/10.1785/0119990161.
Lee, S., Tom, S., Paul, K., 2011. Volcanoes of the World. University of California Press, Berkeley, p. 568.
Lei, B.H., Xu, M., Chen, J.W., Liang, J., Zhang, Y.G., 2018. Structural characteristics and evolution of the South Yellow Sea Basin since Indosinian. China Geol. 1, 466–476. https://doi.org/10.31035/cg2018063.
Lévêque, J.-J., Rivera, L., Wittlinger, G., 1993. On the use of the checker-board test to assess the resolution of tomographic inversions. Geophys. J. Int. 115, 313–318. https://doi.org/10.1111/j.1365-246X.1993.tb05605.x.
Li, C.F., Chen, B., Zhou, Z.Y., 2009. Deep crustal structures of eastern China and adjacent seas revealed by magnetic data. Sci China Ser D Earth Sci 52, 984–993. https://doi.org/10.1007/s11430-009-0096-x.
Li, C.L., Feng, J.K., Fan, J.K., Dong, D.D., Dosso, S.E., 2022. Seismic anisotropy evidence for modified lithosphere below the Bohai Sea region, eastern North China Craton. Tectonophysics 823. https://doi.org/10.1016/j.tecto.2021.229192.
Li, H.L., Gao, R., Huang, X.F., Wang, H.Y., Guo, X.Y., Liang, H.D., Tan, X.M., Liu, X.H., Yang, Z., 2023. Triassic convergence and tectonic evolution of the West Qinling orogen: constraints from reflection-seismology imaging. Gondwana Res. 122, 1–10. https://doi.org/10.1016/j.gr.2023.05.020.
Li, N., Li, W.R., Long, H.Y., 2016. Tectonic evolution of the north depression of the south Yellow Sea basin since late cretaceous. J. Ocean Univ. China 15, 967–976. https://doi.org/10.1007/s11802-016-2843-x.
Li, Q.H., Zhang, Y.S., Kim, S.G., 2007. 3-D crustal velocity tomography in the southern Korean Peninsula. Chin. J. Geophys. 50, 1073–1081 (in Chinese).
Li, S.G., Jagoutz, E., Chen, Y.Z., Li, Q.L., 2000. Sm-Nd and Rb-Sr isotopic chronology and cooling history of ultrahigh pressure metamorphic rocks and their country rocks at Shuanghe in the Dabie Mountains. Central China. Geochim. Cosmochim. Acta 64, 1077–1093. https://doi.org/10.1016/S0016-7037(99)00319-1.
Li, X.P., Yan, J.Y., Schertl, H.P., Kong, F.M., Xu, H., 2014. Eclogite from the Qianliyan Island in the Yellow Sea: a missing link between the mainland of China and the Korean peninsula. Eur. J. Mineral. 26, 727–741. https://doi.org/10.1127/ejm/2014/0026-2403.
Li, Z.X., 1994. Collision between the North and South China Blocks - a Crustal-Detachment Model for Suturing in the Region East of the Tanlu fault. Geology 22, 739–742.
Li, Z.Y., Li, Y.L., Wijbrans, J.R., Yang, Q.J., Qiu, H.N., Brouwer, F.M., 2018. Metamorphic P-T Path differences between the two UHP Terranes of Sulu Orogen, Eastern China: petrologic Comparison between Eclogites from Donghai and Rongcheng. J. Earth Sci. 29, 1151–1166. https://doi.org/10.1007/s12583-018-0845-x.
Liang, R.C., Pei, Y.L., Zheng, Y.P., Wei, J.W., Liu, Y.G., 2003. Gravity and magnetic field and tectonic structure character in the southern Yellow Sea. Chin. Sci. Bull. 48, 64–73. https://doi.org/10.1007/bf02900942.
Lin, W., Wei, W., 2020. Late Mesozoic extensional tectonics in the North China Craton and its adjacent regions: a review and synthesis. Int. Geol. Rev. 62, 811–839. https://doi.org/10.1080/00206814.2018.1477073.
Liu, F.L., Zhang, J., Liu, C.H., 2017. Archean to Paleoproterozoic evolution of the North China Craton: preface. Precambrian Res. 303, 1–9. https://doi.org/10.1016/j.precamres.2017.11.011.
Liu, J.A., Cai, R.H., Pearson, D.G., Scott, J.M., 2019. Thinning and destruction of the lithospheric mantle root beneath the North China Craton: a review. Earth Sci. Rev. 196. https://doi.org/10.1016/j.earscirev.2019.05.017.
Liu, J.W., Wang, Z.M., Xie, F.R., Lv, Y.J., 2013. Seismic hazard assessment for greater North China from historical intensity observations. Eng. Geol. 164, 117–130. https://doi.org/10.1016/j.enggeo.2013.07.002.
Liu, L., Gao, S.S., Liu, K.H., Griffin, W.L., Li, S.Z., Tong, S.Y., Ning, J.Y., 2022. Mantle dynamics of the North China Craton: new insights from mantle transition zone imaging constrained by P-to-S receiver functions. Geophys. J. Int. 231, 629–637. https://doi.org/10.1093/gji/ggac210.
Liu, L.H., Lü, C.C., Hao, T.Y., Zhang, X.H., Kim, K., Kim, H., Guo, Y.G., 2025. Crustal variations and tectonic implications across the South Yellow Sea based on active-source wide-angle seismic analyses. Gondwana Res. 137, 117–130. https://doi.org/10.1016/j.gr.2024.10.001.
Liu, Y.B., Pei, S.P., 2017. Temporal and spatial variation of b-value before and after Wenchuan earthquake and its tectonic implication. Chin. J. Geophys. 60, 2104–2112. https://doi.org/10.6038/cjg20170607 (in Chinese).
Lu, S.N., Yu, H.F., Li, H.K., Chen, Z.H., Wang, H.C., Zhang, C.L., Xiang, Z.Q., 2006. Early Paleozoic suture zones and tectonic divisions in the "Central China Orogen". Geol. Bull. China 25, 1368–1380. https://doi.org/10.3969/j.issn.1671-2552.2006.12.004 (in Chinese).
Lü, Z.Q., Lei, J.S., 2022. Seismic evidence for crustal modification across the Tanlu Fault Zone in Eastern China. Geophys. Res. Lett. 49, e2022GL099761. https://doi.org/10.1029/2022GL099761.
Luo, S., Yao, H.J., Zhang, Z.Q., Bem, T.S., 2022. High-resolution crustal and upper mantle shear-wave velocity structure beneath the central-southern Tanlu fault: implications for its initiation and evolution. Earth Planet. Sci. Lett. 595. https://doi.org/10.1016/j.epsl.2022.117763.
Ma, F., Hou, F.H., Li, T.Y., Wu, Z.Q., Zhang, J.Z., 2023. Crustal velocity structure in the South Yellow Sea revealed by the joint tomographic inversion of reflected and refracted seismic waves. Front. Earth Sci. 10, 1039300. https://doi.org/10.3389/feart.2022.1039300.
Ma, L.X., Xu, T., Ai, Y.S., Yang, J.H., Yang, Y.J., Fan, E.B., Li, L., Hou, J., Dong, W.Y., 2022. Hot lithosphere beneath the northeastern North China Craton detected by ambient noise tomography. Tectonophysics 839. https://doi.org/10.1016/j.tecto.2022.229551.
Meng, Q.R., Zhang, G.W., 1999. Timing of collision of the North and South China blocks: controversy and reconciliation. Geology 27, 123–126.
Niu, Y.L., 2005. Generation and evolution of basaltic magmas: some basic concepts and a hypothesis for the origin of the Mesozoic-Cenozoic volcanism in eastern China. Geol. J. China Univ. 11, 9–46.
Oh, C.W., Kim, S.W., Choi, S.G., Zhai, M.G., Guo, J.H., Krishnan, S., 2005. First finding of eclogite facies metamorphic event in South Korea and its correlation with the Dabie-Sulu collision belt in China. J. Geol. 113, 226–232. https://doi.org/10.1086/427671.
Oh, C.W., 2006. A new concept on tectonic correlation between Korea, China and Japan: histories from the late Proterozoic to cretaceous. Gondwana Res. 9, 47–61. https://doi.org/10.1016/j.gr.2005.06.001.
Oh, C.W., Sajeev, K., Kim, S.W., Santosh, M., 2006. Tectonic evolution of Korean peninsula and adjacent crustal fragments in Asia: Introduction. Gondwana Res. 9, 19–20. https://doi.org/10.1016/j.gr.2005.07.001.
Pang, Y.M., Zhang, X.H., Guo, X.W., Xiao, G.L., Han, Z.Z., 2017a. Basin modeling in the initial stage of exploration: a case study from the North Subbasin of the South Yellow Sea Basin. Acta Oceanolog. Sin. 36, 65–78. https://doi.org/10.1007/s13131-017-1112-1.
Pang, Y.M., Zhang, X.H., Xiao, G.L., Guo, X.W., Wen, Z.H., Wu, Z.Q., Zhu, X.Q., 2017b. Characteristics of Meso-Cenozoic Igneous Complexes in the South Yellow Sea Basin, lower Yangtze Craton of Eastern China and the Tectonic setting. Acta Geol. Sin. 91, 971–987. https://doi.org/10.1111/1755-6724.13319.
Park, S., Hong, T.K., Rah, G., 2021. Seismic Hazard Assessment for the Korean Peninsula. Bull. Seismol. Soc. Am. 111, 2696–2719. https://doi.org/10.1785/0120200261.
Park, S., Hong, T.K., Kim, B., Lee, J., 2023. Role of backbone fault system on earthquake spawning and Geohazards in the Seoul Metropolitan Area. Earth Space Sci. 10, e2022EA002686. https://doi.org/10.1029/2022EA002686.
Peng, P., Mitchell, R.N., Chen, Y., 2022. Earth's one-of-a-kind fault: the Tanlu fault. Terra Nova 34, 381–394. https://doi.org/10.1111/ter.12611.
Petrishchevsky, A.M., 2022. Extension and Strike-Slips in the Crust of the Yellow Sea (Probabilistic Gravity Model). Oceanology 62, 247–257. https://doi.org/10.1134/S0001437022020138.
Qiao, X.F., Zhang, A.L., 2002. North China block, Jiao-Liao-Korea block and Tanlu fault. Geol. China 29, 337–345. https://doi.org/10.3969/j.issn.1000-3657.2002.04.001 (in Chinese).
Qing, Y.S., Zhao, Y.Y., Chen, L.R., Zhao, S.L., 1989. Geology of the Yellow Sea. China Ocean Press, Beijing (in Chinese), p. 236.
Rawlinson, N., Spakman, W., 2016. On the use of sensitivity tests in seismic tomography. Geophys. J. Int. 205, 1221–1243. https://doi.org/10.1093/gji/ggw084.
Ree, J.H., Cho, M.S., Kwon, S.T., Nakamura, E., 1996. Possible eastward extension of Chinese collision belt in South Korea: the Imjingang belt. Geology 24, 1071–1074.

Ren, J.Y., Tamaki, K., Li, S.T., Zhang, J.X., 2002. Late Mesozoic and Cenozoic rifting and its dynamic setting in Eastern China and adjacent areas. Tectonophysics 344, 175–205. https://doi.org/10.1016/S0040-1951(01)00271-2.

Rogers, J.J.W., Santosh, M., 2006. The Sino-Korean craton and supercontinent history: Problems and perspectives. Gondwana Res. 9, 21–23. https://doi.org/10.1016/j.gr.2005.04.001.

Sajeev, K., Jeong, J., Kwon, S., Kee, W.S., Kim, S.W., Komiya, T., Itaya, T., Jung, H.S., Park, Y., 2010. High P-T granulite relicts from the Imjingang belt. South Korea: Tectonic Significance. Gondwana Res. 17, 75–86. https://doi.org/10.1016/j.gr.2009.07.001.

Shen, F.M., Wang, L.F., Barbot, S., Xu, J.H., 2023. North China as a mechanical bridge linking Pacific subduction and extrusion of the Tibetan Plateau. Earth Planet. Sci. Lett. 622. https://doi.org/10.1016/j.epsl.2023.118407.

Shen, W.H., Zhong, Q., Shi, B.P., 2014. Synthetic seismic intensity for historic earthquakes in the North China Plain: implications for the regional seismic hazard. Nat. Hazards 74, 305–323. https://doi.org/10.1007/s11069-014-1195-3.

Song, J.H., Kim, S., Rhie, J., Lee, S.H., Kim, Y., Kang, T.S., 2018. Imaging of lithospheric structure beneath Jeju Volcanic Island by Teleseismic Traveltime Tomography. J. Geophys. Res. Solid Earth 123, 6784–6801. https://doi.org/10.1029/2018JB015979.

Song, J.H., Kim, S., Rhie, J., 2020. Heterogeneous modification and reactivation of a craton margin beneath the Korean Peninsula from teleseismic travel time tomography. Gondwana Res. 81, 475–489. https://doi.org/10.1016/j.gr.2019.11.016.

Straume, E.O., Gaina, C., Medvedev, S., Hochmuth, K., Gohl, K., Whittaker, J.M., Fattah, R.A., Doornenbal, J.C., Hopper, J.R., 2019. GlobSed: Updated Total Sediment Thickness in the World's Oceans. Geochem. Geophys. Geosyst. 20, 1756–1772. https://doi.org/10.1029/2018GC008115.

Sun, Q., 2019. The improvement of double-difference seismic tomography method and its application to the northeastern Tibetan Plateau. (doctoral thesis), University of Chinese Academy of Sciences, Beijing, China (in Chinese). 160 p.

Sun, Q., Pei, S., Cui, Z., Chen, Y.J., Liu, Y., Xue, X., Li, J., Li, L., Zuo, H., 1927. Structure-controlled asperities of the 1920 Haiyuan M8.5 and 1927 Gulang M8 earthquakes, NE Tibet, China, revealed by high-resolution seismic tomography. Sci. Rep. 11, 5090. https://doi.org/10.1038/s41598-021-84642-7.

Sun, Q., Pei, S.P., Cui, Z.X., Chen, Y.J., Liu, Y.B., Xue, X.T., Li, J.W., Li, L., Zuo, H., 2021b. A new growth model of the northeastern Tibetan Plateau from high-resolution seismic imaging by improved double-difference tomography. Tectonophysics 798. https://doi.org/10.1016/j.tecto.2020.228699.

Thurber, C., Eberhart-Phillips, D., 1999. Local earthquake tomography with flexible gridding. Comput. Geosci. 25, 809–818. https://doi.org/10.1016/S0098-3004(99)00007-2.

Thurber, C.H., 1981. Earth structure and earthquake locations in the Coyote Lake area, central California. (doctoral thesis), Massachusetts Institute of Technology, Cambridge, Massachusetts, USA. 332 p.

Tian, Y., Zhao, D.P., 2013. Reactivation and mantle dynamics of North China Craton: insight from P-wave anisotropy tomography. Geophys. J. Int. 195, 1796–1810. https://doi.org/10.1093/gji/ggt333.

Trumbull, R.B., Morteani, G., Li, Z., Bai, H., 1992. Geologic Framework of the Sino-Korean Platform. In: Gold Metallogeny. Springer, Berlin, Heidelberg, pp. 17–55. https://doi.org/10.1007/978-3-642-77350-1_2.

Uno, K., Chang, T.W., Furukawa, K., 2004. Tectonic elements with South China affinity in the Korean Peninsula: new Early Jurassic palaeomagnetic data. Geophys. J. Int. 158, 446–456. https://doi.org/10.1111/j.1365-246X.2004.02299.x.

Waldhauser, F., Ellsworth, W.L., 2000. A double-difference earthquake location algorithm: method and application to the northern Hayward fault. California. Bull. Seismol. Soc. Am. 90, 1353–1368. https://doi.org/10.1785/0120000006.

Wan, T.F., 2001. Distinctive characteristics of Sino-Korean and Yangtze Plates. Geol. Rev. 47, 57–63. https://doi.org/10.3321/j.issn:0371-5736.2001.01.009 (in Chinese).

Wang, J., Zhao, D.P., Yao, Z.X., 2013. Crustal and uppermost mantle structure and seismotectonics of North China Craton. Tectonophysics 582, 177–187. https://doi.org/10.1016/j.tecto.2012.10.004.

Wang, P.X., Li, Q.Y., Li, C.F., 2014. Geology of the China Seas. Elsevier, Amsterdam, 696 p.

Wang, Q., Song, X.D., Ren, J.Y., 2017a. Ambient noise surface wave tomography of marginal seas in East Asia. Earth Planet. Phys. 1, 13–25. https://doi.org/10.26464/epp2017003.

Wang, Q., Sun, W.D., Faure, M., Li, H., 2023. From the Yanshan orogeny to late Mesozoic multi-plate convergence in East Asia. Tectonophysics 856. https://doi.org/10.1016/j.tecto.2023.229839.

Wang, Q.C., Lin, W., 2002. Geodynamics of the dabieshan collisional orogenic belt. Earth Sci. Front. 9, 257–265. https://doi.org/10.3321/j.issn:1005-2321.2002.04.005.

Wang, R., Shi, W.Z., Xie, X.Y., Wang, L.L., Manger, W., Bushey, A.B., Xu, Q.H., 2017b. Lower cretaceous lacustrine successions, North Yellow Sea Basin, eastern China: rift basin sequence stratigraphy and stacking patterns in response to magmatic activity. Mar. Pet. Geol. 88, 531–550. https://doi.org/10.1016/j.marpetgeo.2017.09.006.

Wessel, P., Luis, J.F., Uieda, L., Scharroo, R., Wobbe, F., Smith, W.H.F., Tian, D., 2019. The generic mapping tools version 6. Geochem. Geophys. Geosyst. 20, 5556–5564. https://doi.org/10.1029/2019GC008515.

Whitford-Stark, J.L., 1987. A survey of Cenozoic volcanism on mainland Asia. Geological Society of America, Boulder 213 p. https://doi.org/10.1130/SPE213-p1.

Wong, W.H., 1929. The mesozoic orogenic movement in Eastern China. Bull. Geol. Soc. China 8, 33–44. https://doi.org/10.1111/j.1755-6724.1929.mp8001004.x.

Wu, F.Y., Xu, Y.G., Gao, S., Zheng, J.P., 2008. Lithosphere thinning and destruction of the North China Craton. Acta Petrol. Sin. 24, 1145–1174 (in Chinese).

Wu, Y., 2011. The Structure of the Crust and Upper Mantle in North China Craton from Teleseismic Receiver Function. (doctoral thesis), Institute of Geophysics, China Earthquake Administration, Beijing, China (in Chinese). 120 p.

Xiao, Q.B., Zhao, G.Z., Wang, J.J., Zhan, Y., Chen, X.B., Tang, J., Cai, J.T., Wan, Z.S., Wang, L.F., Ma, W., Zhang, J.H., 2009. Deep electrical structure of the Sulu orogen and neighboring areas. Sci. China Ser. D Earth Sci. 52, 420–430. https://doi.org/10.1007/s11430-009-0013-3.

Xu, J.F., Zhang, B.R., Han, Y.W., 2008. Geochemistry of the Mian-Lue ophiolites in the Qinhng Mountains, central China: constraints on the evolution of the Qinling orogenic belt and collision of the North and South China cratons. J. Asian Earth Sci. 32, 336–347. https://doi.org/10.1016/j.jseaes.2007.11.004.

Xu, J.W., Zhu, G., 1994. Tectonic models of the Tan-Lu fault Zone, Eastern China. Int. Geol. Rev. 36, 771–784. https://doi.org/10.1080/00206819409465487.

Xu, M., Chen, J.W., Liang, J., Zhang, Y.G., Lei, B.H., Shi, J., Wang, J.Q., Liu, J., Liu, H., 2019. Basement structures underneath the northern South Yellow Sea basin (East China): implications for the collision between the North China and South China blocks. J. Asian Earth Sci. 186. https://doi.org/10.1016/j.jseaes.2019.104040.

Xu, P.F., Liu, F.T., Wang, Q.C., Cong, B.L., Chen, H., Sun, R.M., 2000a. Seismic tomography beneath the Dabie-Sulu Collision Orogen - 3D velocity structures of lithosphere. Chin. J. Geophys. 43, 377–385. https://doi.org/10.3321/j.issn:0001-5733.2000.03.011 (in Chinese).

Xu, P.F., Sun, R.M., Liu, F.T., Wang, Q.C., Cong, B.L., 2000b. Seismic tomography showing subduction and slab breakoff of the Yangtze block beneath the Dabie-Sulu orogenic belt. Chin. Sci. Bull. 45, 70–74. https://doi.org/10.1007/bf02884907.

Xu, P.F., 2001. Three-dimensional velocity structure of the lithosphere in the Dabie-Sulu orogenic belt and the eastern part of the North China Block. (postdoctoral thesis), Institute of Geology and Geophysics, Chinese Academy of Sciences, Beijing, China (in Chinese). 78 p.

Xu, P.F., Liu, F.T., Wang, Q.C., Gong, B.L., Chen, H., 2001. Slab-like high velocity anomaly in the uppermost mantle beneath the Dabie-Sulu orogen. Geophys. Res. Lett. 28, 1847–1850. https://doi.org/10.1029/2000GL012187.

Xu, P.F., Zhao, D.P., 2009. Upper-mantle velocity structure beneath the North China Craton: implications for lithospheric thinning. Geophys. J. Int. 177, 1279–1283. https://doi.org/10.1111/j.1365-246X.2009.04120.x.

Xu, X., Zuza, A., Chen, L., Zhu, W.L., Yin, A., Fu, X.W., Gao, S.L., Xu, X.H., Kuang, X.T., Zhang, F.Q., Wu, L., Lin, X.B., Chen, H.L., Yang, S.F., 2021. Late cretaceous to Early Cenozoic extension in the lower Yangtze region (East China) driven by Izanagi-Pacific plate subduction. Earth Sci. Rev. 221. https://doi.org/10.1016/j.earscirev.2021.103790.

Xu, X.W., Han, Z.J., Yang, X.P., Zhang, S.M., Yu, G.H., Zhou, B.G., Li, F., Ma, B.Q., Chen, Z.H., Ran, Y.K., 2016a. Seismotectonic Map of China and its Adjacent Regions. Seismological Press, Beijing (in Chinese), 64 p. Doi: 10.12031/activefault.china.250.2016.db.

Xu, Y., Li, Z.W., Kim, K., Hao, T.Y., Liu, J.S., 2009. Crustal velocity structure and collision boundary between the Sino-Korea and Yangtze blocks in the Yellow Sea. Chin. J. Geophys. 52, 646–652 (in Chinese).

Xu, Y., Zeyen, H., Hao, T.Y., Santosh, M., Li, Z.W., Huang, S., Xing, J., 2016b. Lithospheric structure of the North China Craton: integrated gravity, geoid and topography data. Gondwana Res. 34, 315–323. https://doi.org/10.1016/j.gr.2015.03.010.

Xuan, S.B., Jin, S.G., Chen, Y., 2020. Determination of the isostatic and gravity Moho in the East China Sea and its implications. J. Asian Earth Sci. 187. https://doi.org/10.1016/j.jseaes.2019.104098.

Yang, F., Santosh, M., Kim, S.W., Zhou, H.Y., Jeong, Y.J., 2019. Late Mesozoic intraplate rhyolitic volcanism in the North China Craton: far-field effect of the westward subduction of the Paleo-Pacific Plate. Geol. Soc. Am. Bull. 132, 291–309. https://doi.org/10.1130/b35123.1.

Yang, J.H., O'Reilly, S., Walker, R.J., Griffin, W., Wu, F.Y., Zhang, M., Pearson, N., 2010. Diachronous decratonization of the Sino-Korean craton: Geochemistry of mantle xenoliths from North Korea. Geology 38, 799–802. https://doi.org/10.1130/G30944.1.

Yang, L.Q., Deng, J., Dilek, Y., Qiu, K.F., Ji, X.Z., Li, N., Taylor, R.D., Yu, J.Y., 2015. Structure, geochronology, and petrogenesis of the late Triassic Puziba granitoid dikes in the Mianlue suture zone, Qinling orogen, China. Geol. Soc. Am. Bull. 127, 1831–1854. https://doi.org/10.1130/B31249.1.

Yang, S.Y., Jung, H.S., Lim, D.I., Li, C.X., 2003. A review on the provenance discrimination of sediments in the Yellow Sea. Earth Sci. Rev. 63, 93–120. https://doi.org/10.1016/S0012-8252(03)00033-3.

Ye, G.F., Liu, C., Luo, X., Jin, S., Wei, W.B., Dong, H., Yin, Y.T., 2021. Dynamical significance of the Tanlu Fault Zone in the destruction of the North China Craton: the evidence provided by the three-dimensional Magnetotelluric array study. Tectonophysics 813. https://doi.org/10.1016/j.tecto.2021.228910.

Yin, A., Nie, S.Y., 1993. An Indentation model for the north and south china collision and the development of the Tan-Lu and Honam Fault systems, Eastern Asia. Tectonics 12, 801–813. https://doi.org/10.1029/93TC00313.

Yin, Q.H., Ma, P.F., Li, X.P., 2016. Investigation of northeast extension and geological evolution of the Sulu-Dabie high-pressure metamorphic belt. Adv. Geosci. 6, 201–213. https://doi.org/10.12677/ag.2016.63023.

Zhai, M.G., Guo, J.H., Li, Z., Chen, D.Z., Peng, P., Li, T.S., Hou, Q.L., Fan, Q.C., 2007. Linking the Sulu UHP belt to the Korean Peninsula: evidence from eclogite, Precambrian basement, and Paleozoic sedimentary basins. Gondwana Res. 12, 388–403. https://doi.org/10.1016/j.gr.2007.02.003.

Zhai, M.G., 2016. Comparative study of geology in North China and Korean Peninsula: research advances and key issues. Acta Petrol. Sin. 32, 2915–2932 (in Chinese).

Zhai, M.G., Zhang, X.H., Zhang, Y.B., Wu, F.Y., Peng, P., Li, Q.L., Li, Z., Guo, J.H., Li, T.S., Zhao, L., Zhou, L.G., Zhu, X.Y., 2019. The geology of North Korea: an overview. Earth Sci. Rev. 194, 57–96. https://doi.org/10.1016/j.earscirev.2019.04.025.

Zhang, H.J., Thurber, C., 2005. Adaptive mesh seismic tomography based on tetrahedral and Voronoi diagrams: application to Parkfield, California. J. Geophys. Res. Solid Earth 110, B04303. https://doi.org/10.1029/2004JB003186.

Zhang, H.J., Thurber, C., 2006. Development and applications of double-difference seismic tomography. Pure Appl. Geophys. 163, 373–403. https://doi.org/10.1007/s00024-005-0021-y.

Zhang, K.J., 1997. North and South China collision along the eastern and southern North China margins. Tectonophysics 270, 145–156. https://doi.org/10.1016/S0040-1951(96)00208-9.

Zhang, L.M., Shu, P.Y., Teng, C.K., Chen, H.X., 1985. Is Tanlu fault belt an active seismic zone. Chin. J. Geophys. 28, 230–232 (in Chinese).

Zhang, M.H., Xu, D.S., Chen, J.W., 2007. Geological structure of the yellow sea area from regional gravity and magnetic interpretation. Appl. Geophys. 4, 75–83. https://doi.org/10.1007/s11770-007-0011-1.

Zhang, P., Yao, H.J., Chen, L., Fang, L.H., Wu, Y., Feng, J.K., 2019. Moho depth variations from receiver function imaging in the Northeastern North China craton and its tectonic implications. J. Geophys. Res. Solid Earth 124, 1852–1870. https://doi.org/10.1029/2018JB016122.

Zhang, P.Z., Deng, Q.D., Zhang, G.M., Ma, J., Gan, W.J., Min, W., Mao, F.Y., Wang, Q., 2003. Active tectonic blocks and strong earthquakes in the continent of China. Sci China Ser D Earth Sci 46, 13–24. https://doi.org/10.1360/03dz0002.

Zhang, R.Y., Liou, J.G., Ernst, W.G., 2009. The Dabie-Sulu continental collision zone: a comprehensive review. Gondwana Res. 16, 1–26. https://doi.org/10.1016/j.gr.2009.03.008.

Zhang, R.Y., Yang, F.L., Hu, P.P., Yang, X.D., Peng, Y.X., 2021. Cenozoic tectonic inversion in the Northern Depression, South Yellow Sea Basin, East Asia: structural styles and driving mechanism. Tectonophysics 798. https://doi.org/10.1016/j.tecto.2020.228687.

Zhang, T., Zhu, W.L., Fu, Q., Fu, X.W., 2022. Structural characteristics and tectonic evolution of the Wunansha Uplift in the South Yellow Sea Basin, China. Geofluids 2022, 1565978. https://doi.org/10.1155/2022/1565978.

Zhao, C., Zhang, J., Wang, X., Zhang, C., Chen, G.K., Zhang, S.H., Guo, M.J., 2023. Tracing the Early Crustal Evolution of the North China Craton: new Constraints from the Geochronology and Hf Isotopes of Fuchsite Quartzite in the Lulong Area Eastern Hebei Province. Minerals 13, 1174. https://doi.org/10.3390/min13091174.

Zhao, G.C., Li, S.Z., Sun, M., Wilde, S.A., 2011. Assembly, accretion, and break-up of the Palaeo-Mesoproterozoic Columbia supercontinent: record in the North China Craton revisited. Int. Geol. Rev. 53, 1331–1356. https://doi.org/10.1080/00206814.2010.527631.

Zhao, G.C., Cawood, P.A., Li, S.Z., Wilde, S.A., Sun, M., Zhang, J., He, Y.H., Yin, C.Q., 2012. Amalgamation of the North China Craton: Key issues and discussion. Precambrian Res. 222, 55–76. https://doi.org/10.1016/j.precamres.2012.09.016.

Zhao, L.F., Xie, X.B., Wang, W.M., Zhang, J.H., Yao, Z.X., 2013. Crustal Lg attenuation within the North China Craton and its surrounding regions. Geophys. J. Int. 195, 513–531. https://doi.org/10.1093/gji/ggt235.

Zhao, L.F., Xie, X.B., Wang, W.M., Yao, Z.X., 2018. A broadband crustal Lg wave attenuation model in Northeast China and the Korean Peninsula. Chin. J. Geophys. 61, 856–871. https://doi.org/10.6038/cjg2018L0394 (in Chinese).

Zhao, W.A., Liu, C.G., Liu, K., Li, G.B., Wu, Z.Q., Zhi, P.Y., 2024. P-wave velocity structure of the Sulu orogenic belt in the Yellow Sea, East China: evidence from wide-angle ocean-bottom seismograph data. Geophys. Prospect. 72, 1452–1469. https://doi.org/10.1111/1365-2478.13357.

Zhao, X.X., Coe, R.S., Chang, K.H., Park, S.O., Omarzai, S.K., Zhu, R.X., Zhou, Y.X., Gilder, S., Zheng, Z., 1999. Clockwise rotations recorded in early cretaceous rocks of South Korea: implications for tectonic affinity between the Korean Peninsula and North China. Geophys. J. Int. 139, 447–463. https://doi.org/10.1046/j.1365-246X.1999.00944.x.

Zheng, J.P., Xia, B., Dai, H.K., Ma, Q., 2020. Lithospheric structure and evolution of the North China Craton: an integrated study of geophysical and xenolith data. Sci. China Earth Sci. 64, 205–219. https://doi.org/10.1007/s11430-020-9682-5.

Zheng, Q.G., Cai, L.G., Ding, W.L., Lu, Y.D., Cao, Q.G., 2005. Development and evolution of basins in Yellow Sea. Oil Gas Geol. 647–654. https://doi.org/10.11743/ogg20050515 (in Chinese).

Zheng, T.Y., Zhao, L., Zhu, R.X., 2009. New evidence from seismic imaging for subduction during assembly of the North China craton. Geology 37, 395–398. https://doi.org/10.1130/G25600a.1.

Zhu, A.L., XU, X.W., Wang, P., Ren, Y., Sun, D.J., 2018. The present activity of the central and southern segments of the Tancheng-Lujiang Fault Zone evidenced from relocated microseismicity and focal mechanisms. Earth Sci. Front. 25, 218–226. https://doi.org/10.13745/j.esf.yx.2016-11-54 (in Chinese).

Zhu, G., Hu, Z.-Q., Chen, Y., Niu, M.-I., Xie, C.-L., 2008. Evolution of Early cretaceous extensional basins in the eastern North China craton and its implication for the craton destruction. Geol. Bull. China 27, 1594–1604 (in Chinese).

Zhu, G., Niu, M.L., Xie, C.L., Wang, Y.S., 2010. Sinistral to Normal Faulting along the Tan-Lu Fault Zone: evidence for Geodynamic Switching of the East China Continental Margin. J. Geol. 118, 277–293. https://doi.org/10.1086/651540.

Zhu, G., Jiang, D.Z., Zhang, B.L., Chen, Y., 2012a. Destruction of the eastern North China Craton in a backarc setting: evidence from crustal deformation kinematics. Gondwana Res. 22, 86–103. https://doi.org/10.1016/j.gr.2011.08.005.

Zhu, R.X., Chen, L., Wu, F.Y., Liu, J.L., 2011. Timing, scale and mechanism of the destruction of the North China Craton. Sci. China Earth Sci. 54, 789–797. https://doi.org/10.1007/s11430-011-4203-4.

Zhu, R.X., Xu, Y.G., Zhu, G., Zhang, H.F., Xia, Q.K., Zheng, T.Y., 2012b. Destruction of the North China Craton. Sci. China Earth Sci. 55, 1565–1587. https://doi.org/10.1007/s11430-012-4516-y.

Zhu, W.Q., Beroza, G.C., 2019. PhaseNet: a deep-neural-network-based seismic arrival-time picking method. Geophys. J. Int. 216, 261–273. https://doi.org/10.1093/gji/ggy423.

Zou, Z.H., Liu, K., Zhao, W.N., Liu, H.S., Zhou, H.W., Meng, X.J., Li, Y., Gurrola, H., 2016. Upper crustal structure beneath the northern South Yellow Sea revealed by wide-angle seismic tomography and joint interpretation of geophysical data. Geol. J. 51, 108–122. https://doi.org/10.1002/gj.2847.